Research Article | Open Access

Journal of Materials Informatics

Gao *et al. J. Mater. Inf.* **2026**, *6*, 53 **DOI:**10.20517/jmi.2026.50

Smart design tungsten-weighted refractory high entropy alloys (WW-RHEAs) under dynamic loading

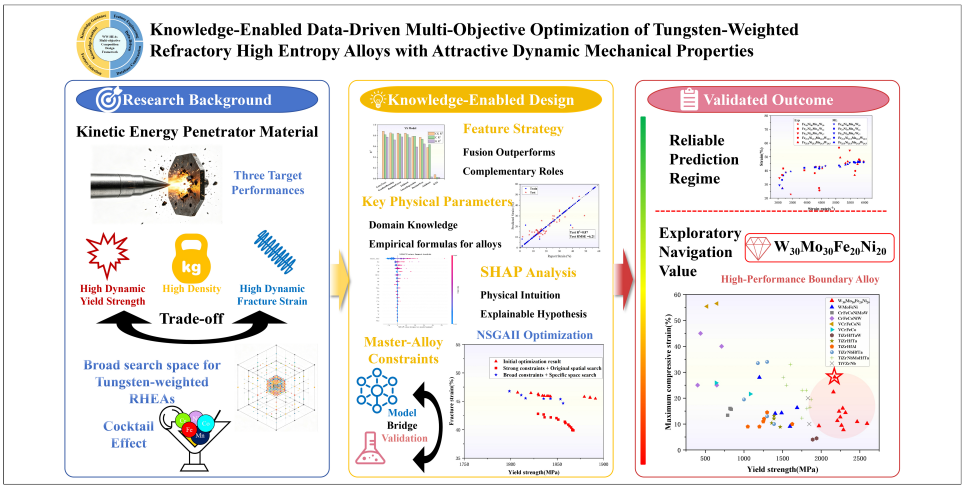
Yusu Gao[1], Dian Jia[1,2], Ruiyue Zhang[1], Yijing Fan[3], Yu Tang[3,*], William Yi Wang[1,2,*], Shuxin Bai[3], Jinshan Li[1,2,*]

Keywords:
Refractory high-entropy alloys, tungsten alloy, machine learning, multi-objective optimization, dynamic mechanical properties

Citation: Gao, Y.; Jia, D.; Zhang, R.; Fan, Y.; Tang, Y.; Wang, W. Y.; Bai, S.; Li, J. Smart design tungsten-weighted refractory high entropy alloys (WW-RHEAs) under dynamic loading. *J. Mater. Inf.* **2026**, *6*, 53. https://dx.doi.org/10.20517/jmi.2026.50

Received: 7 Jul 2026
First Decision: 17 Aug 2026
Revised: 17 Sep 2026
Accepted: 30 Sep 2026
Published: 29 Oct 2026

Academic Editor:
Xingjun Liu
Copy Editor:
Pei-Yun Wang
Production Editor:
Pei-Yun Wang



Abstract

Tungsten-weighted refractory high-entropy alloys (WW-RHEAs) are refractory high-entropy alloys containing W as a major constituent to achieve high density. Through composition tuning, these alloys can simultaneously satisfy the requirements of high density, high strength, and plasticity in dynamic impact environments. The development of WW-RHEAs faces critical challenges, including insufficient interpretability of data-driven machine learning models for predicting the unique dynamic behavior of such alloys, as well as the multi-objective optimization problem arising from the persistent strength-ductility trade-off. To address these challenges, this study constructed an intelligent design framework, termed machine learning-based multi-objective strategy (MMOS), which integrates the philosophy of being knowledge-enabled and data-driven. By integrating both physical parameters and composition as feature variables, the designed "composition and knowledge" fusion model demonstrated strong performance in predicting dynamic yield strength and fracture strain, achieving test the coefficient of determination values of 0.96 for strength and 0.87 for fracture strain. Through three iterative optimization rounds, each performing 250,000 objective evaluations on hypothetical compositions, the framework

Check for updates

[1]State Key Laboratory of Solidification Processing, Northwestern Polytechnical University, Xi'an 710072, Shaanxi, China.
[2]Innovation Center, NPU Chongqing, Chongqing 401135, China.
[3]College of Aerospace Science and Engineering, National University of Defense Technology, Changsha 410073, Hunan, China.

***Correspondence to:** Prof. William Yi Wang, Prof. Jinshan Li, State Key Laboratory of Solidification Processing, Northwestern Polytechnical University, Xi'an 710072, Shaanxi, China. E-mail: wywang@nwpu.edu.cn; ljsh@nwpu.edu.cn; Prof. Yu Tang, College of Aerospace Science and Engineering, National University of Defense Technology, Changsha 410073, Hunan, China. E-mail: tangyu16@zju.edu.cn

efficiently navigated the compositional space. The Pareto-optimal as-cast alloy $W_{30}Mo_{30}Fe_{20}Ni_{20}$ in the W-Mo-Fe-Ni system was identified by the optimization framework as a promising candidate and experimentally characterized by split Hopkinson pressure bar experiments. This alloy exhibits a dynamic compressive yield strength of 2,174 MPa and a maximum compressive strain of 25% attained before unloading at a strain rate of 2,054 s^{-1} under high-strain-rate dynamic compression, demonstrating an attractive combination of strength and ductility in the dynamic compression regime. The results demonstrate the effectiveness of MMOS in efficiently exploring the composition space while incorporating practical fabricability considerations, and highlight its knowledge-enabled capability in enhancing the interpretability of predictive models.

INTRODUCTION

To maintain structural integrity under dynamic impact, structural materials must possess both high strength and sufficient ductility under dynamic loading. In kinetic-energy armor-piercing applications, materials require high-density metallic elements such as tungsten heavy alloys (WHAs)[1-4] and depleted uranium alloys[5-7] to carry sufficient kinetic energy and enable controlled shear localization for effective penetration. WHAs typically suffer from a mushrooming effect at the penetrator head, resulting in inferior penetration performance compared to depleted uranium alloys[8,9], which however raise environmental contamination concerns[10]. To overcome these limitations, tungsten-weighted refractory high-entropy alloys (WW-RHEAs) have recently emerged as a promising alternative. Based on the multi-principal element concept, this class of materials incorporates tungsten alongside other refractory and transition metals as co-principal elements, breaking the conventional single-principal-element design paradigm. The "multi-principal element" characteristic endows WW-RHEAs with a unique "cocktail effect"[11], offering high tunability in composition and properties. The same design philosophy has also inspired other advanced structural materials, such as lightweight Fe-Mn-Al-Ni-C compositionally complex steels[12]. Theoretically, WW-RHEAs provide a novel platform for the synergistic optimization of dynamic strength, ductility, and density, and thus serve as potential candidates for future high-density dynamic applications worthy of further investigation.

Since the first report of single-phase body-centered cubic (BCC) structured RHEAs, interest in RHEAs has grown exponentially[13]. Significant advances in mechanical properties have been reported for RHEAs. By activating diverse deformation mechanisms such as kink bands[14-17], edge dislocations[18], deformation twins[19-21], and introducing heterogeneous microstructures (e.g., B2/L12 nanoprecipitates[15,20,22], spinodal decomposition[15], dual-phase structures[23]), RHEAs have demonstrated notable strength-ductility synergy under both quasi-static and dynamic conditions[14-16,19,20,24-26]. For instance, through specific microstructural design and thermomechanical processing, alloys have been reported with dynamic yield strength exceeding 2 GPa and uniform strain up to ~30% under high strain rates[20], or quasi-static yield strength around 1.4 GPa with ~20% tensile ductility[25]. These properties are closely linked to key physical parameters such as valence electron concentration (VEC)[16-18,27], lattice distortion[17,18,25,26,28], and generalized stacking fault energy (GSFE)[16,17,29]. Numerous alloys have been evaluated both theoretically and experimentally; however, the efficiency of this compositional search has remained low[30]. The vast compositional space limits the feasibility of exhaustive experimentation. Traditional high-entropy alloy (HEA) design methods often rely on empirical approaches and trial-and-error experiments, which are time-consuming and resource-intensive[31-33]. Emerging artificial intelligence (AI) technologies provide new methodologies for data analysis, pattern recognition, and optimization in the HEA research field, enhancing the efficiency and accuracy of the HEA design process[34,35]. Utilizing machine learning (ML) algorithms[36,37] and predictive modeling, AI technologies can rapidly explore large materials databases and assist in identifying promising HEA compositions and properties[38-42]. This emerging trend underscores the potential of AI-driven computational approaches to transform HEA research and accelerate the development of advanced materials with tailored properties for diverse applications[43,44]. Furthermore, based on existing ML models, leveraging

multi-objective optimization algorithms for compositional design[45-49] enables the efficient screening of optimal solutions from the vast compositional space that simultaneously satisfy multiple objectives and constraints. Recent reviews have also highlighted the growing importance of integrating multi-objective optimization with ML in materials discovery[50].

While search efficiency has been significantly improved by current purely data-driven material screening frameworks, such frameworks still suffer from inherent limitations in interpretability. These frameworks heavily rely on "black-box" complex ML models with opaque internal decision logic and limited interpretability[51]. The models can only provide performance predictions but fail to elucidate which key physical factors are responsible for achieving high performance. Such a black-box nature makes it difficult for researchers to extract verifiable scientific mechanisms or formulate universal material design principles from the predictions.

To address this, recent studies have begun integrating domain-knowledge features into ML models, achieving both high prediction accuracy [e.g., the coefficient of determination (R^2) > 0.9] and enhanced mechanistic interpretability[38,40,41,49]. This physics-informed approach transforms models from opaque predictors into interpretable tools. For instance, models like DuctGPT incorporate electronic-structure descriptors to predict ductility[40], whereas other work focuses on establishing the direct theoretical relationships that underpin such descriptors[49,52]. Additionally, although existing multi-objective optimization studies have made significant progress in synergistically optimizing strength and ductility[53,54], partially overcoming this traditional trade-off, the optimization objectives are typically confined to mechanical properties alone. In practical application scenarios such as kinetic energy penetration, material density is a critical factor, as it correlates strongly with both momentum-carrying capacity and resistance to adiabatic shear banding[19,55]. Studies on RHEAs confirm that high-density elements are crucial for dynamic performance[14-17,19,23,25,26,56], underscoring the need to expand optimization objectives beyond strength-ductility trade-offs to include application-specific metrics like density.

In this work, the machine learning-based multi-objective strategy (MMOS) framework is established. By systematically evaluating three feature strategies, composition-only, knowledge-only, and fusion of the two, and employing SHapley Additive exPlanations (SHAP) analysis to reveal model-based feature associations and generate physically plausible interpretations, the framework achieves both high predictive accuracy and interpretability. The optimal composition + knowledge fusion model achieves test R^2 values of 0.96 for dynamic yield strength and 0.87 for fracture strain. Through three iterative optimization rounds with progressively refined exploration strategies, each performing 250,000 objective evaluations on hypothetical compositions, the framework efficiently navigates the compositional space and converges to Pareto-optimal candidates. The Pareto-optimal alloy $W_{30}Mo_{30}Fe_{20}Ni_{20}$ is identified and experimentally characterized via split Hopkinson pressure bar (SHPB) testing, achieving a dynamic compressive yield strength of 2,174 MPa and a maximum compressive strain of 25% at a strain rate of 2,054 s^{-1}. This work builds upon a previous knowledge-enabled study[57], where key performance parameters (KPPs) for dynamic properties were identified. While the previous work focused on single-target prediction, the present work goes beyond by: (i) integrating KPPs with compositional features to construct ML models compatible with multi-objective optimization; (ii) embedding master-alloy constraints (Fe:Ni = 1:1, W:Mo = 1:1) directly into the Non-dominated Sorting Genetic Algorithm II (NSGA-II) framework[58] to improve practical fabricability; (iii) completing a full design-and-validation cycle through SHPB testing of Pareto-optimal candidates, a step not undertaken in prior computational screening studies; and (iv) explicitly delineating the applicability domain for the model by reporting both successful validations and boundary deviations, providing a transparent foundation for future iterative refinement.

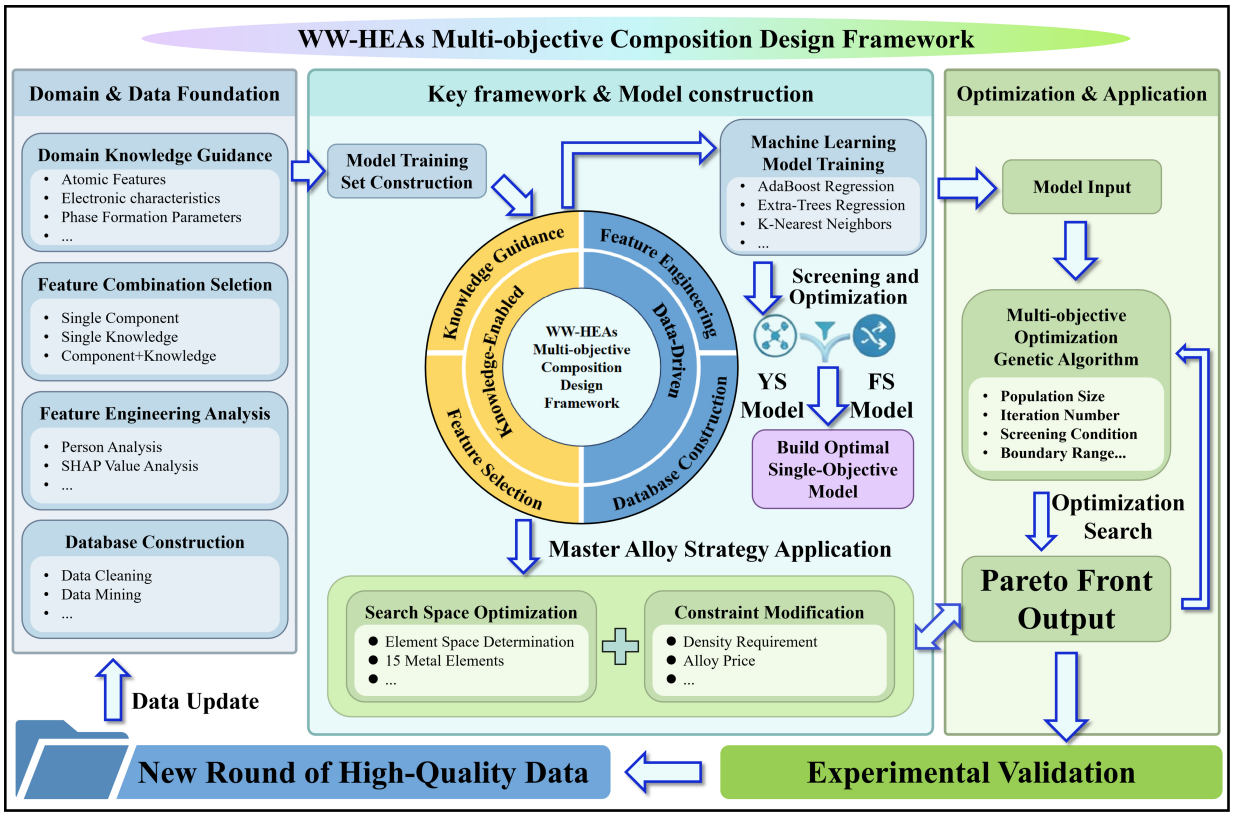


Figure 1. Knowledge-enabled, data-driven multi-objective compositional design framework for W-weighted refractory high-entropy alloys based on a master alloy strategy. The "Data Update → New Round of High-Quality Data" pathway represents a future closed-loop iteration paradigm and was not implemented in the present study. The current work completes a full design-and-validation cycle without model retraining using the newly generated experimental data. WW-HEAs: Tungsten-weighted high-entropy alloys; SHAP: SHapley Additive exPlanations; YS: yield strength; FS: fracture strain.

MATERIALS AND METHODS

Multi-objective compositional design framework for high-entropy alloys

As shown in Figure 1, the present study introduces a knowledge-enabled, data-driven multi-objective compositional design framework for WW-RHEAs based on a master alloy strategy. The framework aims to identify candidate alloys with favorable properties. It primarily consists of three main steps: data-driven, knowledge-enabled model training; multi-objective optimization based on the master alloy strategy; and experimental validation.

High-quality data serves as the foundation for developing high-performance ML models. Therefore, during the data collection phase, the primary focus was on gathering experimental data pertaining to the composition, yield strength, and fracture strain of high-entropy alloys at specific strain rates. Furthermore, this framework incorporates the concept of knowledge enablement, meaning the entire data collection process was guided by domain-specific expertise in the field of material dynamic impact.

The features required for training the ML models need to be determined through feature engineering. Feature engineering involves identifying and selecting the most relevant features from high-dimensional material datasets to enhance the predictive capability of the ML models. Regarding model selection, single-target models for the objective properties were first established based on the results of feature engineering, utilizing different feature sets and various ML algorithms. Subsequently, these models were optimized, and the predictive performances were compared. The optimal single-target models based on the "composition",

"domain knowledge", and "composition + domain knowledge" feature sets, respectively, were retained. These models were then applied within a multi-objective optimization algorithm to search for optimal compositions within the compositional space, thereby providing a basis for further screening and selecting the most suitable model.

Considering the practical fabricability of refractory high-entropy alloys, the master alloy strategy is employed to impose composition constraints, specifically equiatomic ratios between certain element pairs (Fe:Ni = 1:1 and W:Mo = 1:1). These constraints avoid the direct melting of pure elements with largely different melting points, thereby reducing the risk of segregation and element loss during arc melting. These constraints are intended to improve melt compatibility and facilitate synthesis; however, successful fabrication of every generated composition is not guaranteed, and such fabrication may additionally depend on phase stability and other processing factors. The master alloy strategy thus serves as a practical means to incorporate fabricability considerations while maintaining an efficient search over the compositional space. Based on this strategy, the multi-objective optimization algorithm achieves the maximization of multiple target properties and the regulation of multiple constraints, while simultaneously maintaining consideration for practical applicability.

Finally, candidate alloys identified from the Pareto front are experimentally characterized. The resulting experimental data are retained as an independent validation set, and the empirical basis for subsequent model refinement is provided by the data, though the data have not been used for model retraining in the present study.

Construction of multi-objective optimization database for high-entropy alloys

Database construction and data mining

In ML, a feature represents an independent, observable attribute or characteristic of an observed object, and multiple features collectively form a feature vector. The dataset used in this work was derived from the data of a previous study[57], underwent certain processing steps, and ultimately comprised experimental data points. To comprehensively consider feature parameters related to dynamic performance and enhance model interpretability, both material composition information and key domain knowledge were employed to generate features during database construction. Consequently, a comprehensive multi-component high-entropy alloy database containing 23 features was developed.

The raw data collection included both dynamic compression and dynamic tension records from the literature, totaling 312 data points. Since the present study focuses exclusively on dynamic compressive properties, all tension records (64 data points) were objectively excluded; no further filtering based on performance values or trends was applied. The final database therefore comprises 248 data points (compression only), covering 51 unique RHEA compositions from 46 source publications. All 248 records contain complete information for both dynamic yield strength and fracture strain, yielding 248 yield-strength and 248 fracture-strain records. Among these 248 records, 159 (≈ 64%) correspond to the as-cast state, which is the processing condition of primary interest for the present work; the remaining 89 (≈ 36%) records include thermomechanically processed or annealed states. The database covers strain rates from 400 to 6,000 s^{-1}, with dynamic yield strengths ranging from approximately 500 to 2,500 MPa and fracture strains varying between 5% and over 60%. Although some source publications (listed in Supplementary Table 1) reported test conditions extending beyond 6,000 s^{-1}, the specific compression records extracted from those publications and included in the present training database are all within the 400-6,000 s^{-1} range. No additional performance- or trend-based filtering was applied beyond the objective exclusion of dynamic tension records (64 data points), as noted above. The compositional space encompasses 18 elements, including refractory metals (W, Mo, Hf, Ta, Nb, Zr), transition metals (Ti, V, Cr, Fe, Co, Ni, Cu, Mn), the light element Al, the non-metallic elements (Si, O), and minor additions of the rare-earth element Gd.

Table 1. Physical descriptors used as domain-knowledge features

Parameters	Formula
Shear modulus	$G = \sum c_i G_i$
Young's modulus	$E = \sum c_i E_i$
Bulk modulus	$B = \sum c_i B_i$
Pugh's ratio	$B/G = \sum c_i B_i / \sum c_i G_i$
Thermal conductivity	$\lambda = \sum c_i \lambda_i$
Density	$\rho = \sum c_i M_i / \sum (c_i M_i / \rho_i)$

Elemental values of shear modulus (G), Young's modulus (E), bulk modulus (B), thermal conductivity (λ), and density (ρ) used in the above mixing rules were taken from the CRC Handbook of Chemistry and Physics, 107th ed.[62].

Construction of feature repositories under three strategies

The domain-knowledge features employed in this work, including shear modulus (G), thermal conductivity (λ), Young's modulus (E), Pugh's ratio (B/G), and strain rate, were adopted from a prior investigation on knowledge-enabled ML for dynamic properties of high-entropy alloys[57]. The formulas and calculation methods for these physical descriptors are summarized in Table 1. These descriptors are intended as heuristic indicators of the underlying physical tendencies (e.g., ductile-brittle character or thermal transport behavior) and are evaluated collectively through the predictive performance of the ML models. The selection of these features reflects the physical linkage to the three core mechanisms governing dynamic mechanical behavior: dislocation motion resistance, adiabatic heating, and ductile-brittle transition. Rather than performing exhaustive feature engineering, the present work focuses on systematically evaluating three feature strategies (composition-only, knowledge-only, and fusion) and embedding the optimal models into a multi-objective optimization framework with experimental validation.

Genetic algorithms are employed for multi-objective optimization of alloy composition. In this framework, each candidate alloy composition is encoded as an individual, and crossover and mutation operations directly modify the elemental fractions to generate new candidates. The algorithm iteratively searches the composition space guided by the objective function values evaluated by the ML models.

The simplest method to train models based on this principle is to use composition directly as the feature parameter. After crossover and mutation, these compositional features are normalized and then directly employed to train and optimize the model. The advantage of this approach is that it simplifies the program flow and reduces code complexity. The selection of domain-knowledge features (e.g., shear modulus, Pugh's ratio) was guided by established empirical knowledge and phenomenological constitutive models related to dynamic deformation mechanisms, as evidenced in prior work[57]. These physically meaningful descriptors, which have demonstrated effectiveness in correlating with mechanical properties, were adopted in the present study to construct interpretable models within the multi-objective optimization framework.

Therefore, the domain knowledge features used therein can be directly referenced to establish multi-objective optimization models. Throughout the optimization process, the genes of each individual remain the elemental composition. After a new individual is generated by crossover and mutation of the composition, predefined formulas are used to calculate the domain knowledge features of this individual, followed by the multi-objective optimization workflow. In this context, ML models are trained using three distinct feature compositions: composition features alone, domain knowledge features alone, and a fusion of both. The feature vectors correspondingly consist of "composition", "domain knowledge", or a combination

of both. Since expert domain knowledge features are incorporated, this approach provides interpretability for the multi-objective optimization model. In summary, when conducting multi-objective optimization using these three methods, the genes constituting the alloy individuals remain the elemental composition of the alloy. However, the input–output mapping of the ML models differs across the three strategies: from composition only, from domain knowledge only, or from the fusion to the prediction target(s).

The present work does not aim to discover new physical descriptors through exhaustive feature engineering, as reported in recent titanium alloy studies[59]. Instead, established domain-knowledge features, shear modulus (G), thermal conductivity (λ), Young's modulus (E), Pugh's ratio (B/G), and strain rate, derived from the prior investigations on the dynamic deformation of high-entropy alloys, are built upon[57]. These features are physically linked to dislocation motion resistance, adiabatic heating, and ductile-brittle transition, the three core mechanisms governing dynamic mechanical behavior. The contribution of the present work lies in systematically evaluating three feature strategies, namely composition-only (C), knowledge-only (K), and composition + knowledge (CK), across eight ML algorithms and two target properties, and in embedding the optimal models into a multi-objective optimization framework with experimental validation.

Construction and evaluation of ML models

In this work, the following eight ML regression algorithms were employed: tree-based ensemble algorithms, including adaptive boosting (AdaBoost), gradient boosting (GradientBoosting), decision tree, extremely randomized trees (ExtraTrees), random forest, and eXtreme gradient boosting (XGBoost); and other algorithms, namely K-nearest neighbors (KNN) and linear regression. The dataset was partitioned into a training set (80%) and a test set (20%). Fifty rounds of resampling were performed, and prediction models were subsequently trained with yield strength and fracture strain as the respective targets. Evaluation metrics are crucial for assessing the performance of ML models. Model performance is reflected in its predictive and generalization capabilities, and different performance criteria can lead to varying judgments. Therefore, in regression prediction tasks, evaluating the predictive ability of a model involves comparing its predictions with the actual values. Key metrics include R^2, mean absolute error (MAE), mean squared error, root mean squared error, mean absolute percentage error (MAPE), and mean bias error, among others. The primary metrics utilized in this work are as follows[60]:

R^2, also known as the goodness of fit, indicates a better fitting performance of the evaluation model when its value is closer to 1, and a poorer fit when closer to 0. Generally, an R^2 value greater than 0.8 is considered indicative of a good model fit. It is defined as $R^2 = 1 - \frac{\sum_{i=1}^{m}(y_i - \hat{y}_i)^2}{\sum_{i=1}^{m}(y_i - \bar{y})^2}$.

The MAE is the average of the absolute differences between the true values and the predicted values across all sample instances. It effectively reflects the error between predictions and actual values. MAE is a linear score where all individual differences are weighted equally in the average. It is defined as $MAE = \frac{1}{m}\sum_{i=1}|y_i - \hat{y}_i|$.

The MAPE is calculated by dividing the difference between the actual and predicted values by the actual value, increasing linearly with the error magnitude. MAPE is scale-independent, expressed as a percentage with a constant dimension, making it easy to understand and avoiding the issue of positive and negative errors canceling each other out. It is defined as $MAPE = \frac{1}{m}\sum_{i=1}^{m}\frac{|y_i - \hat{y}_i|}{y_i} \times 100\%$.

Hyperparameter optimization was conducted after training the model with the base algorithm. It aims to enhance the generalization ability of the model, prevent overfitting, and assess model feasibility by adjusting hyperparameter values, thereby achieving the desired outcome. Grid search and cross-validation are employed as common model optimization methods: the former systematically explores a predefined parameter range, while the latter divides the training set into K subsets (K = 5 is used in this work). In each iteration, K-1 subsets are used for training, and the remaining one subset is used for validation. This process is repeated K times, and the final validation error is the average of the K results. By applying cross-validation to train and validate all parameter combinations within the grid search, the parameter combination yielding the lowest cross-validation error is ultimately selected and applied to the model. For the prediction models targeting strength and ductility based on the "composition", "domain knowledge", and "composition + domain knowledge" feature sets, each model was adjusted using a specific set of hyperparameters, and the combination resulting in the smallest prediction error was chosen as the final model.

Establishment of multi-objective optimization algorithm

Multi-objective optimization problems (MOOPs) involve two or more conflicting objective functions. In materials design, optimizing one property often comes at the expense of another; for instance, improving strength typically reduces ductility. Therefore, the solution involves finding the best compromise among competing objectives.

Pareto optimality describes a state of optimal resource allocation where no objective can be improved without degrading another. The Pareto front represents the set of all such non-dominated solutions. Two key concepts in NSGA-II are non-dominated sorting, which ranks individuals based on dominance relationships, and crowding distance, which measures the density of individuals within a population to maintain diversity. It is defined as $d_i = \sum_{m=1}^{M} \frac{|f_m^{i+1} - f_m^{i-1}|}{f_m^{max} - f_m^{min}}$, with Min-Max normalization per objective and infinite distance assigned to boundary individuals to preserve extreme Pareto solutions.

The methods for solving MOOPs can be categorized into two major types: scalarization methods, such as the weight coefficient method, which transform the multi-objective problem into a single-objective one; and genuine multi-objective optimization algorithms, which directly address trade-offs among multiple objectives.

In the field of evolutionary computation, numerous classical intelligent optimization algorithms have been extended to address multi-objective problems. This work employs the NSGA-II[58], which has become one of the benchmark algorithms in this field due to its efficiency. NSGA-II incorporates an elitist strategy to preserve superior solutions across generations and uses crowding distance to ensure solution diversity, thereby achieving both convergence and coverage of the Pareto front. Density was estimated using the formula given in Table 1. A study-specific minimum estimated-density threshold of 10 g/cm^3 was adopted as an engineering screening criterion to bias the search toward higher-density candidates. During the non-dominated sorting and Pareto extraction steps, individuals with estimated density below this threshold were assigned invalid objective values (-1, -1) and were excluded from the final Pareto front. This ensures that all reported Pareto-optimal solutions satisfy this estimated-density criterion, while allowing the evolutionary search to explore the full composition space without premature restrictions.

The NSGA-II algorithm was implemented with POP_SIZE = 500 and GEN_NUM = 500 per iteration, with XOVR = 0.8 (crossover probability) and Pm = 0.2 (mutation probability). Each iteration thus performed POP_SIZE × GEN_NUM = 250,000 objective evaluations on hypothetical compositions. To identify practically meaningful candidates, a two-step deduplication procedure was applied to the final

Pareto-optimal solutions: compositions with identical elemental fractions (within 0.1 at.%) were first consolidated programmatically; the remaining candidates were then manually inspected and consolidated based on compositional similarity to avoid redundant experimental validation. A pragmatic similarity guideline was adopted: compositions differing by ≤ 0.1 at.% per element and by ≤ 1 at.% in total content of W and Mo were considered similar and were consolidated to a single representative composition for experimental validation.

Experimental validation

The RHEA ingots were synthesized through vacuum arc-melting under a high-purity argon atmosphere. Following five re-melts for chemical homogeneity, the molten alloy was suction-cast into a water-cooled copper mold to produce cuboid specimens (10 × 10 × 60 mm^3). Cylindrical compression samples with dimensions of Φ5 × 3 mm were machined via electrical discharge machining with ±0.02 mm dimensional tolerance. Dynamic compression tests were conducted using an SHPB system. Triplicate tests were performed for each strain-rate condition, with rates ranging from approximately 2,000 to 5,000 s^{-1} for the primary test matrix, and additional validation tests were conducted at higher strain rates up to approximately 6,000 s^{-1} to further probe the dynamic response. Stress-strain curves were derived through one-dimensional stress wave analysis[61], with strain rates calculated from incident/reflected wave signals. For specimens lacking photographic evidence of fracture, the reported maximum values represent the highest stress and strain achieved before experimental unloading, not necessarily the intrinsic failure limits of the material. Such values are designated as ε_{max} throughout this work, whereas "fracture strain" is reserved exclusively for specimens with documented macroscopic cracking.

RESULTS AND DISCUSSION

High predictive accuracy and interpretability of the knowledge-fused ML model

Systematic evaluation of three feature strategies

As summarized in Figures 2 and 3, the CK fusion model generally achieves superior predictive performance compared to the C-only and K-only strategies, particularly for the more competitive ensemble algorithms such as ExtraTrees, Random Forest, and GradientBoosting. For instance, in dynamic yield strength prediction, the CK-ExtraTrees model achieves a test R^2 of 0.883 with root mean square error (RMSE) = 196 MPa, outperforming the best C-only model (R^2 = 0.834, GradientBoosting) and the best K-only model (R^2 = 0.777, random forest). However, CK is not universally dominant across all algorithms; for weaker learners such as KNNs and decision tree, the performance differences among the three feature strategies are marginal and inconsistent. Nevertheless, since the ExtraTrees algorithm with the CK feature set yields the highest predictive accuracy among all evaluated models, it is selected as the optimal model for subsequent hyperparameter optimization and multi-objective integration. This focused selection ensures that the best-performing combination, rather than a universally superior strategy, drives the downstream optimization.

These contrasting rankings carry significant implications. For strength prediction, composition-only models perform reasonably well ($R^2 \approx 0.83$), whereas in the titanium alloy system reported by Liu *et al.*[59], composition-only models yielded substantially lower performance (test $R^2 \approx 0.12$ for strength). This discrepancy originates from the more direct correlation between elemental composition and strengthening effects in refractory multi-principal element alloys. In WW-RHEAs, the significant atomic size differences among constituent elements (W, Mo, Fe, Ni, *etc.*) are known to contribute to solid-solution strengthening, making composition a reasonably effective predictor for yield strength. For ductility prediction, however, composition-only models fail ($R^2 \approx 0.40$), while knowledge features substantially improve performance ($R^2 \approx 0.57$). This disparity indicates that fracture strain under dynamic loading is governed by complex, synergistic mechanisms, dislocation motion, adiabatic heating, and phase stability, that are better captured by physically meaningful descriptors than by raw composition alone.

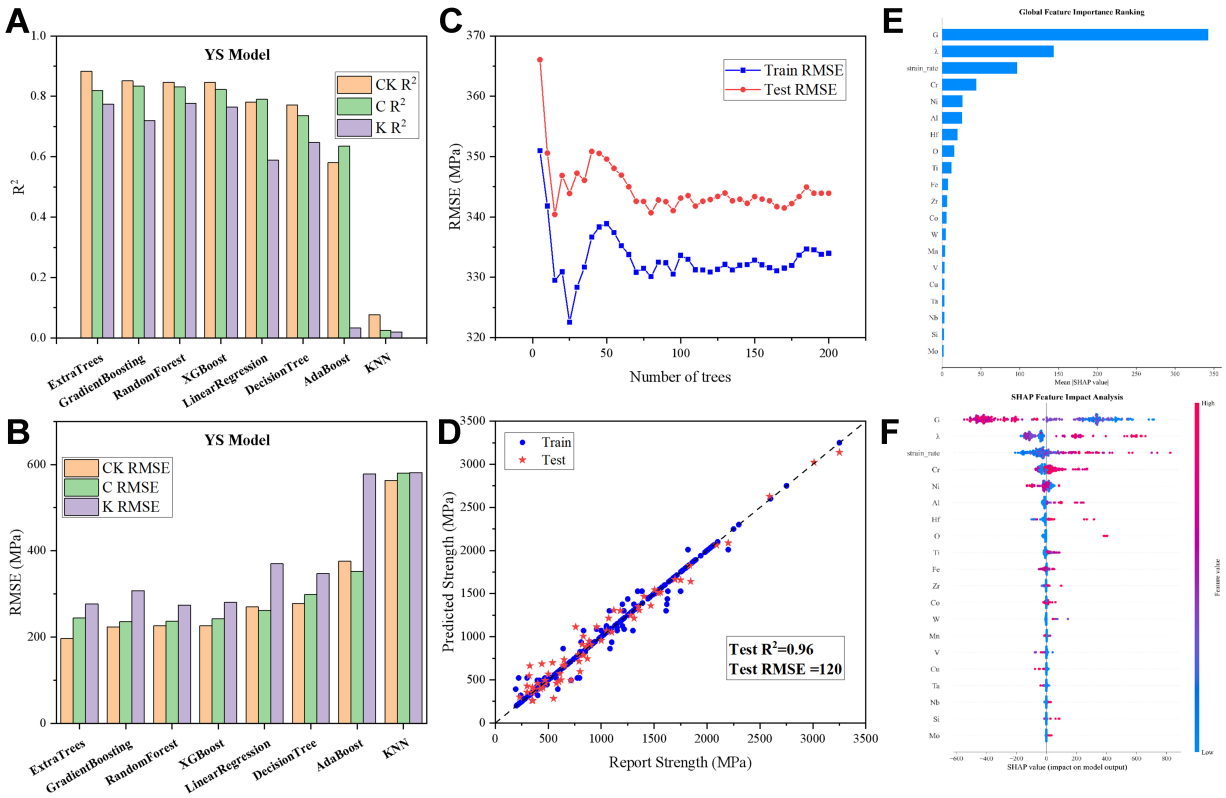


Figure 2. Performance comparison of eight ML models for strength datasets constructed based on "composition", "domain knowledge", and "composition + domain knowledge" strategies, and analysis of the importance of SHAP values of the features. (A) and (B) are respectively the R^2 and RMSE results of the 8 fitted ML models on the test sets after 50 resampling iterations; (C) Convergence of test RMSE as a function of the number of decision trees for the ExtraTrees model built on the "composition + domain knowledge" feature set; (D) is the fitting plot of the optimal ExtraTrees model for the strength dataset constructed based on "composition + domain knowledge" after hyperparameter optimization; (E) and (F) are the bar chart and swarm chart for the importance analysis of the SHAP features of the strength dataset constructed based on "composition + domain knowledge", respectively. ML: Machine learning; SHAP: SHapley Additive exPlanations; R^2: the coefficient of determination; RMSE: root mean square error; ExtraTrees: extremely randomized trees; YS: yield strength; GradientBoosting: gradient boosting; RandomForest: random forest; XGBoost: eXtreme gradient boosting; Linear: linear regression; DecisionTree: decision tree; AdaBoost: adaptive boosting; KNN: K-nearest neighbors.

Model hyperparameter optimization and final performance

Based on the systematic evaluation of the three feature strategies, the ExtraTrees algorithm with the CK fusion feature set was selected as the optimal model for both strength and ductility predictions. To further enhance performance and ensure robust generalization, hyperparameter optimization was conducted using a grid search strategy combined with five-fold cross-validation. The parameter space, including n_estimators, max_depth, and min_samples_split, was systematically explored, with the combination yielding the lowest cross-validation error selected for the final model.

The optimized ExtraTrees model for dynamic yield strength achieves a test R^2 of 0.96 with RMSE = 120 MPa [Figure 2D]. For fracture strain, the optimized model achieves a test R^2 of 0.87 with RMSE = 6.21% [Figure 3D]. The comparatively lower performance for ductility prediction reflects the inherently higher stochasticity of fracture strain under dynamic loading, which is governed by a complex interplay of dislocation motion, adiabatic heating, and crack initiation, mechanisms that are more challenging to capture from compositional and physical descriptors alone.

The convergence curves of test RMSE with respect to the ensemble size [Figure 2C and 3C] further confirm model robustness. Both models exhibit rapid convergence, with the test error stabilizing after approximately 50 decision trees and remaining flat as the tree count increases. This flat trend indicates that further

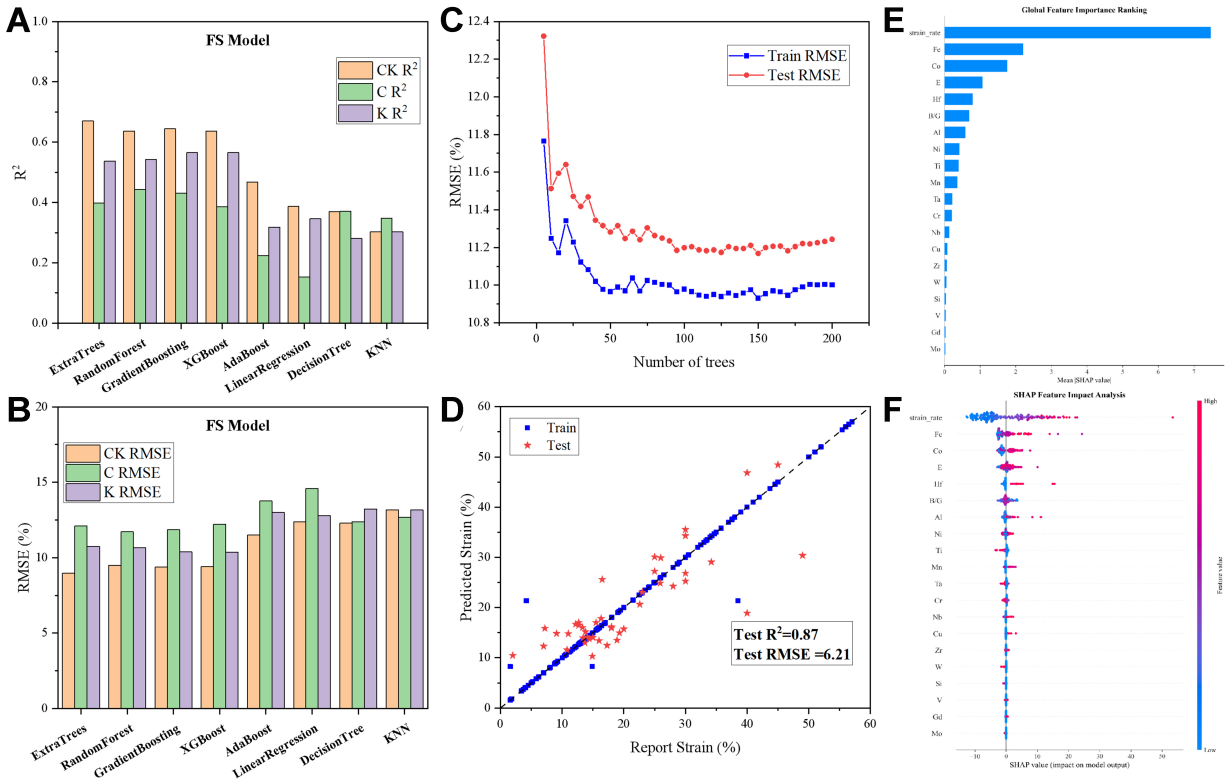


Figure 3. Performance comparison of eight ML models for fracture-strain datasets constructed based on "composition", "domain knowledge", and "composition + domain knowledge" strategies, and analysis of the importance of SHAP values of the features. (A) and (B) are respectively the R^2 and RMSE results of the 8 fitted ML models on the test sets after 50 resampling iterations; (C) Convergence of test RMSE as a function of the number of decision trees for the ExtraTrees model built on the "composition + domain knowledge" feature set; (D) is the fitting plot of the optimal ExtraTrees model for the fracture-strain dataset constructed based on "composition + domain knowledge" after hyperparameter optimization; (E) and (F) are the bar chart and swarm chart for the importance analysis of the SHAP features of the fracture-strain dataset constructed based on "composition + domain knowledge", respectively. ML: Machine learning; SHAP: SHapley Additive exPlanations; R^2: the coefficient of determination; RMSE: root mean square error; ExtraTrees: extremely randomized trees; FS: fracture strain; RandomForest: random forest; GradientBoosting: gradient boosting; XGBoost: eXtreme gradient boosting; AdaBoost: adaptive boosting; Linear: linear regression; DecisionTree: decision tree; KNN: K-nearest neighbors.

increasing the number of trees does not introduce overfitting, suggesting that the hyperparameter-optimized ExtraTrees models have learned stable patterns within the sampled data domain, though the record-level random split does not guarantee generalization to entirely unseen compositions or processing conditions.

SHAP analysis: model-based feature importance and physically plausible interpretations

To move beyond "black-box" predictions, SHAP analysis was performed to quantify the contribution of each feature to the model predictions and to assess whether the model behavior aligns with established physical principles. It is important to emphasize that statistical associations within the trained model are revealed by SHAP values, and physical causality is not independently established by SHAP values. The following interpretations are therefore offered as model-consistent hypotheses that warrant further experimental and theoretical verification.

Strength model [Figure 2E and F]: Shear modulus (G) emerges as the dominant feature, with a mean |SHAP| value of 342.6. Samples with high G are concentrated in the positive SHAP region, which is qualitatively consistent with the greater resistance of high-modulus alloys to shear deformation. However, G is a composition-weighted average and is not a direct descriptor of local lattice distortion. The SHAP-derived association should therefore be interpreted as a model-based correlation with elastic stiffness, not as direct

evidence of a specific strengthening mechanism. Thermal conductivity ranks second (mean |SHAP| = 143.6): samples with low thermal conductivity cluster in the positive region, indicating that reduced heat dissipation may facilitate localized thermal softening, while within the studied strain-rate regime it may also contribute to strain-rate hardening by limiting dynamic recovery; the net effect depends on the competition. It is recognized that under near-adiabatic high-rate loading, low thermal conductivity may also promote thermal softening and strain localization. The net effect on flow stress depends on the competition among strain hardening, strain-rate strengthening, and thermal softening. The SHAP-derived association should therefore be interpreted as a model-based trend rather than a definitive mechanistic conclusion. Strain rate ranks third (mean |SHAP| = 96.9), which is consistent with the expected positive strain-rate sensitivity of flow stress in dynamic compression, although this trend is model-derived and does not independently confirm a specific hardening mechanism.

Notably, compositional features such as Cr, Ni, and Al also show substantial contributions, with mean |SHAP| values of 44.1, 26.5, and 25.7, respectively. Cr exhibits a narrow-band positive distribution, which is consistent with a stable linear strengthening contribution, possibly related to solid-solution effects. Ni and Al show more distributed patterns: the effect of Ni is concentration-dependent, while Al exhibits an olive-shaped distribution, suggesting an optimal compositional window beyond which excessive Al may promote brittle phase formation. Hf (mean |SHAP| = 19.8) and O (mean |SHAP| = 15.7) also contribute meaningfully: the contribution of Hf may be associated with its large atomic radius and the resulting lattice distortion, although this interpretation remains model-derived and requires further experimental verification, and O contributes through interstitial strengthening, although Hf was subsequently excluded from the optimization system due to cost considerations. This result is consistent with the necessity of retaining compositional features in the strength model, a finding that distinguishes this work from titanium alloy systems where composition-only features were reported to be substantially less effective. The feature importance ranking suggests that both electronic-structural descriptors (G, thermal conductivity) and compositional identity show strong associations with accurate strength prediction in RHEAs.

Ductility model [Figure 3E and F]: Strain rate is the most influential feature (mean |SHAP| = 7.47), suggesting a strong association with fracture strain under dynamic loading. Fe and Co follow with mean |SHAP| values of 2.21 and 1.76, respectively. Notably, Young's modulus (E) (mean |SHAP| = 1.07) and B/G (mean |SHAP| = 0.69), the classic Pugh's ductile-brittle criterion, appear as key physical descriptors. High B/G values are concentrated in the positive SHAP region, suggesting that when B/G exceeds the critical threshold, shear deformation may become energetically more favorable, which is in line with the classical Pugh criterion but should be interpreted as a model-derived association. Young's modulus shows an olive-shaped distribution: samples with moderate E cluster in the positive region, suggesting that excessively high E suppresses dislocation nucleation, while low E reduces the elastic energy storage capacity required for sustained plastic deformation.

Hf (mean |SHAP| = 0.79) and Al (mean |SHAP| = 0.59) also contribute to ductility predictions. The SHAP contribution of Hf may be associated with its strong lattice distortion effect, which can promote uniform deformation by activating multiple slip systems. Al exhibits a negative correlation in the swarm plot: samples with high Al content cluster in the negative SHAP region, suggesting an embrittlement risk at elevated Al concentrations, consistent with its tendency to promote ordered intermetallic formation. Compositional features such as Fe and Co exhibit bimodal distributions, indicating that the effects on ductility depend on specific alloying synergies rather than monotonic linear behavior. The SHAP results show that ductility predictions are strongly associated with knowledge features, particularly strain rate, Young's modulus, and B/G, suggesting that these physically meaningful descriptors are useful for capturing the complex interplay of deformation mechanisms under dynamic loading. While individual physical descriptors each capture distinct

mechanisms (e.g., B/G for brittle-ductile tendency, Young's modulus for elastic energy capacity, thermal conductivity for adiabatic heating), the compositional features remain essential for resolving the non-uniqueness problem in the composition-to-descriptor mapping.

The SHAP analysis suggests two key trends: (i) knowledge features show strong associations with ductility prediction, while composition-only features show substantially weaker associations in this model; and (ii) compositional features show strong associations with strength prediction in RHEAs, reflecting the dominant role of solid-solution strengthening effects associated with compositional variations. This mechanism-dependent importance of feature selection underscores that no single "universal" feature strategy exists, the optimal approach must be tailored to the target property and alloy system. The knowledge-enabled interpretability of the model offers physically plausible hypotheses for the subsequent multi-objective search, potentially steering optimization toward regions that are not only performant but also interpretable in terms of established materials-science principles.

Multi-objective optimization and constraint-driven screening of Pareto-optimal WW-RHEAs

Virtual composition space and optimization strategy

Based on the SHAP analysis in Section "SHAP analysis: model-based feature importance and physically plausible interpretations", which identified Cr, Ni, and Al as significant contributors to strength, and Fe, Co, and Hf as influential for ductility, a virtual compositional space was defined for multi-objective optimization. The optimization was designed as a joint search over composition and loading condition, reflecting the fact that strain rate is an intrinsic service parameter in dynamic impact applications. The feature importance rankings, along with elemental frequency, price, and density distributions within the dataset [Figure 4], were used to guide the subsequent selection and exclusion of elements. To ensure both physical relevance and practical fabricability, the following constraints were imposed: (i) Hf was excluded due to its high cost, despite its substantial SHAP contribution to both strength and ductility; (ii) Al was eliminated because its excessively high melting point difference with W may increase the risk of segregation and element loss during arc melting; and (iii) W and Mo were mandatorily retained to favor high-density candidate designs. This yielded a nine-element search space comprising Ti, Cr, Fe, Co, Ni, Zr, Nb, W, and Mo, with atomic fractions for each element bounded between 0 and 35 at.%, and the strain rate ranging from 0 to 5,000 s^{-1} [Table 2]. The objective functions were defined as maximizing both dynamic yield strength and fracture strain, subject to the constraint that all compositions sum to unity.

Pareto frontier comparison across three feature strategies and system convergence

To evaluate the impact of different feature strategies on optimization outcomes, the NSGA-II algorithm was driven by predictive models trained on three distinct feature sets, composition-only (C), knowledge-only (K), and composition + knowledge (CK), to generate the respective Pareto frontiers.

As shown in Figure 5, the three strategies yield markedly different Pareto fronts. The K-only model produces an excessively homogeneous set of Pareto solutions, because the lower-dimensional physical feature space, compared to the vast compositional space, often leads the algorithm to associate "optimal" performance with a narrow range of physical parameters, while the reverse mapping to composition is non-unique and may not be practically realizable. The C-only model yields a broader Pareto front in the performance space, yet its "black-box" nature obscures the physical rationale behind the predicted properties, resulting in a lack of interpretability. In contrast, the CK fusion model achieves the optimal balance: it generates a high-quality Pareto solution set covering a wide range in both strength and ductility while, by virtue of the domain-knowledge features, associating each optimal composition with physically meaningful descriptors such as shear modulus and B/G. This approach unifies the breadth of data-driven exploration with the depth of physical knowledge.

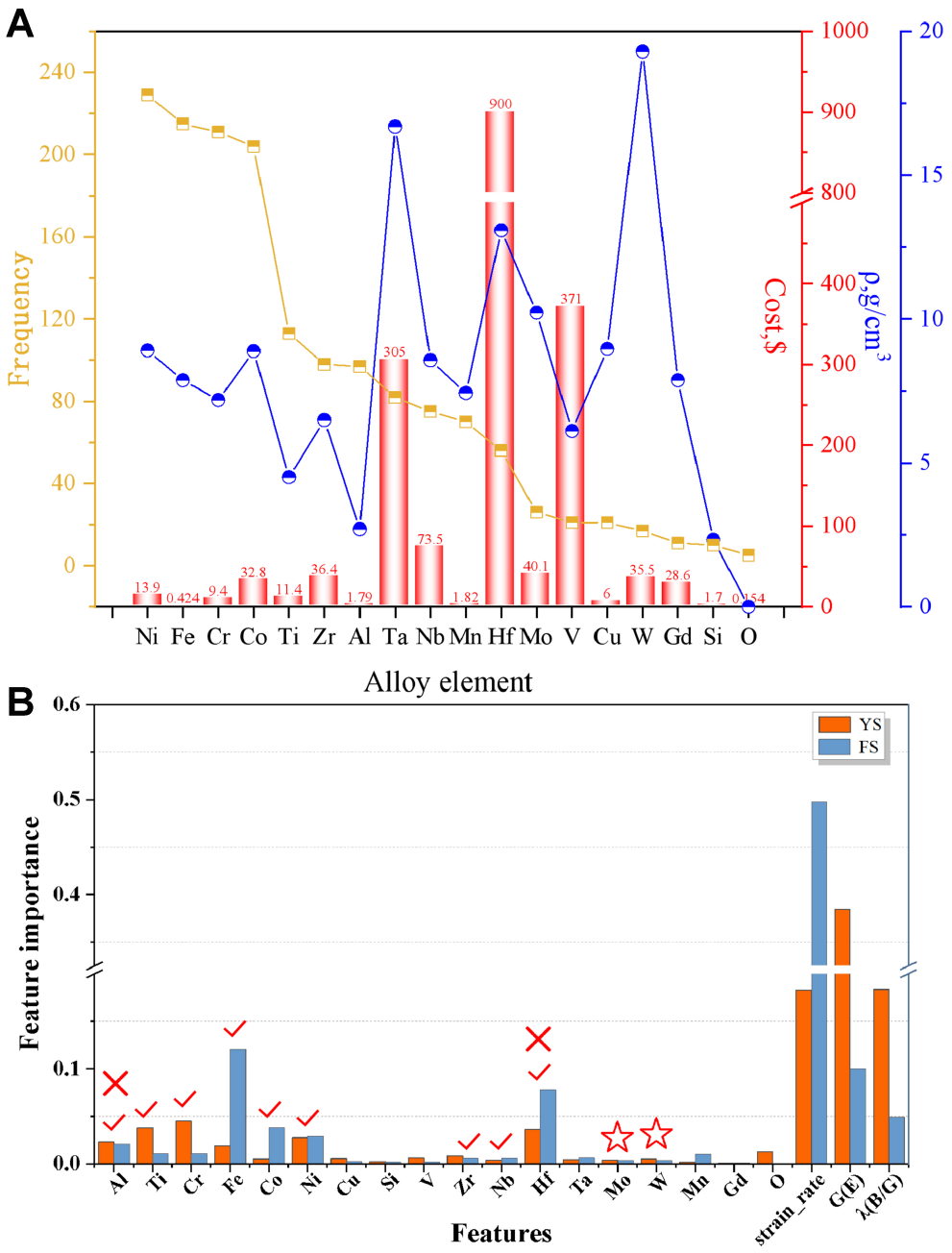


Figure 4. (A) Frequency of occurrence, estimated elemental price (USD/kg), and density contribution of each element in the dataset; (B) Ranking of feature importance for compositional and domain-knowledge characteristics of alloys. Check marks denote elements retained in the virtual composition space for multi-objective optimization; crosses denote elements excluded due to prohibitive cost (Hf), melting point mismatch with tungsten (Al), or increased computational dimensionality without sufficient justification; red five-pointed stars mark Mo and W, which were mandatorily retained to favor high-density candidate designs. YS: Yield strength; FS: fracture strain.

Elemental distribution trends within the CK-derived Pareto front [Figures 6 and 7] reveal the compositional evolution underlying the strength-ductility trade-off. As alloys shift from the high-ductility region to the high-strength region (i.e., with increasing yield strength), the concentrations of elements such as Cr, Fe, Co, and Ni generally decrease, whereas the proportions of Ti, W, Mo, Nb, and Zr increase or remain high. This observed compositional pattern is qualitatively consistent with the expected roles of refractory elements in solid-solution strengthening, but direct mechanistic confirmation (e.g., via phase analysis or electron microscopy) is beyond the scope of the present optimization study. The Pareto front visually demonstrates

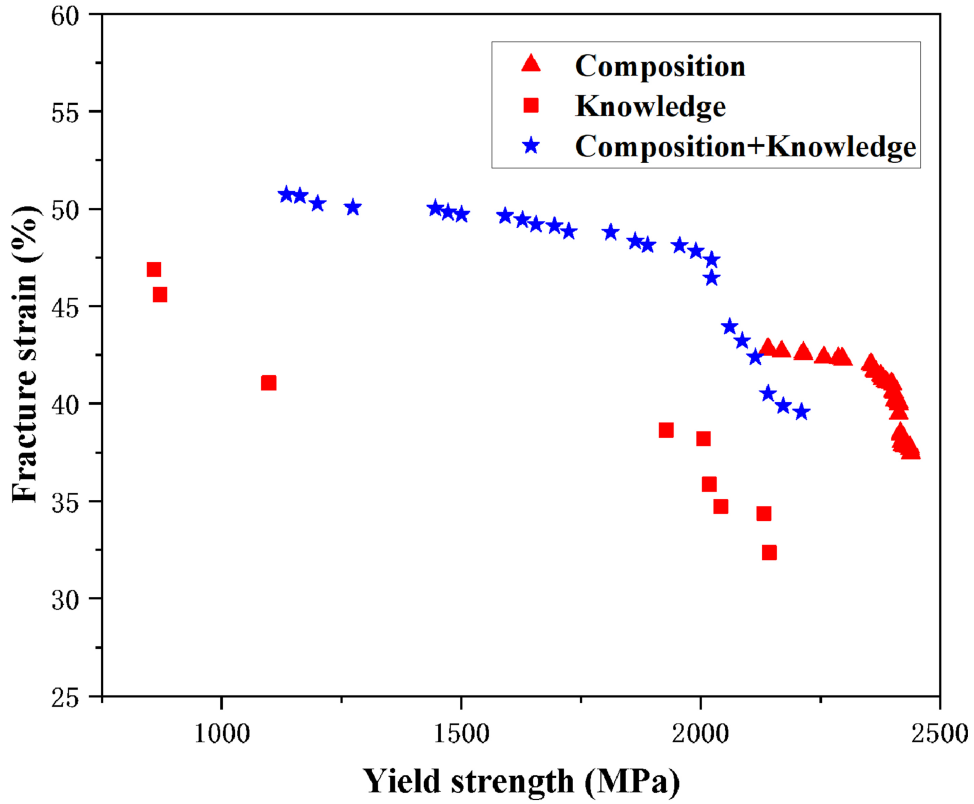


Figure 5. Multi-objective optimization of the Pareto frontier solution set based on three feature strategies.

Table 2. Upper and lower bounds of virtual composition space established for each element and strain rate

Element	Lower bounds	Upper bounds	Element	Lower bounds	Upper bounds
Al	0	0	Zr	0	0.35
Ti	0	0.35	Nb	0	0.35
Cr	0	0.35	Hf	0	0
Fe	0	0.35	Ta	0	0
Co	0	0.35	Mo	0	0.35
Ni	0	0.35	W	0	0.35
Cu	0	0	Mn	0	0
Si	0	0	Gd	0	0
V	0	0	O	0	0
Strain rate	0	5000			

Element bounds are given in atomic fraction.

the competition and compromise between these two categories. Notably, W and Mo appear with high frequency across all Pareto solutions, directly satisfying the pre-defined high-density constraint and indicating the effectiveness of the optimization framework in translating application requirements into compositional preferences. Simultaneously, strain rate within the optimal solution set is predominantly concentrated near 5,000 s^{-1}, aligning with the general principle of strain-rate hardening in dynamic compression.

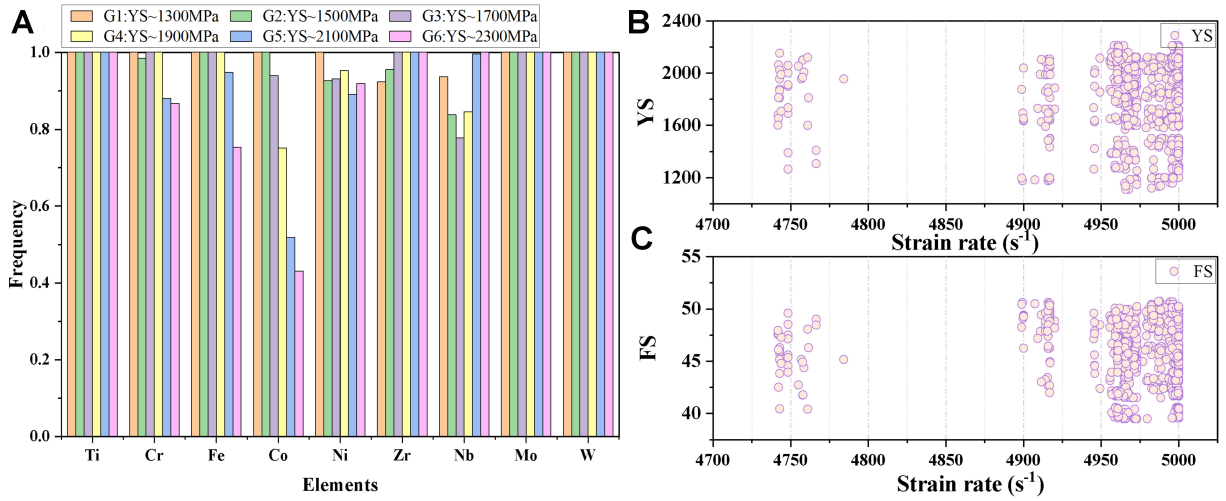


Figure 6. In Pareto frontier alloys: (A) grouping based on values of yield strength and frequency of occurrence of elements in each group; relationship between strain rate and (B) yield strength and (C) fracture strain. YS: Yield strength; FS: fracture strain.

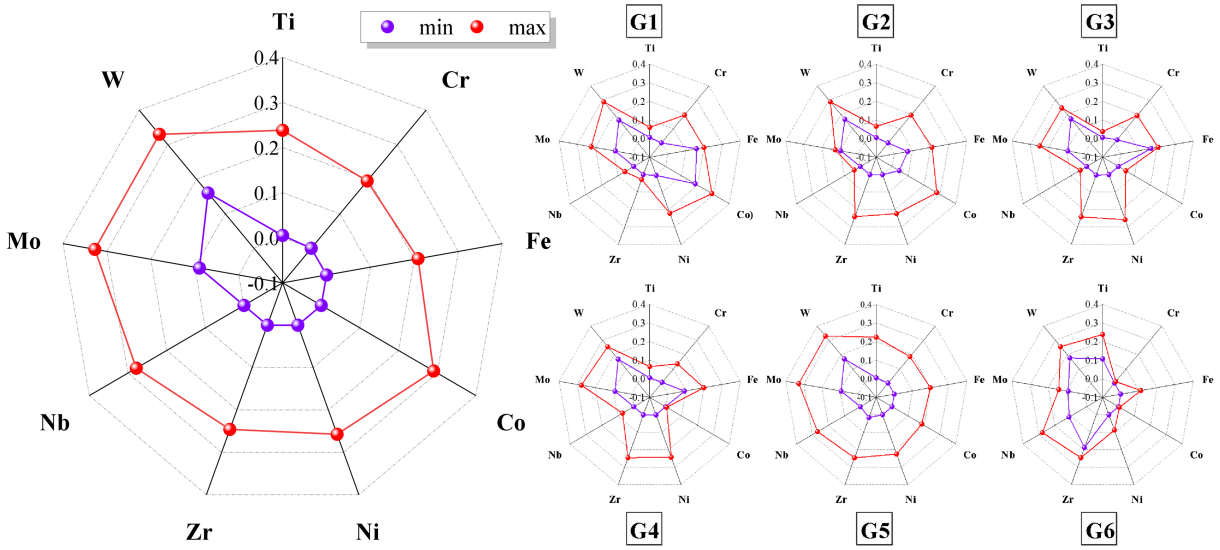


Figure 7. For the Pareto frontier alloys, group classifications and the occurrence probabilities of constituent elements are presented for each strength level (G1-G6), corresponding to ~1,300, ~1,500, ~1,700, ~1,900, ~2,100, and ~2,300 MPa, respectively.

This compositional trend analysis guided the convergence of the optimization system from the initial nine-element space toward the W-Mo-Fe-Ni quaternary system [Figure 8]. While the Ti-W-Mo-Nb-Zr system is capable of achieving excellent strength-ductility synergy, the W-Mo-Fe-Ni system offers superior ductility potential at considerable strength levels, and its simpler composition, coupled with the reported potential[3] of W-heavy alloys for kinetic-energy penetrators, though this aspect is beyond the scope of the present dynamic-compression study, lays the groundwork for subsequent application-oriented investigations. The convergence to this system, however, introduces a fabricability challenge: the vast melting-point difference between W/Mo and Fe/Ni constitutes an inherent barrier for conventional arc melting, motivating the introduction of composition constraints in the iterative optimization that follows.

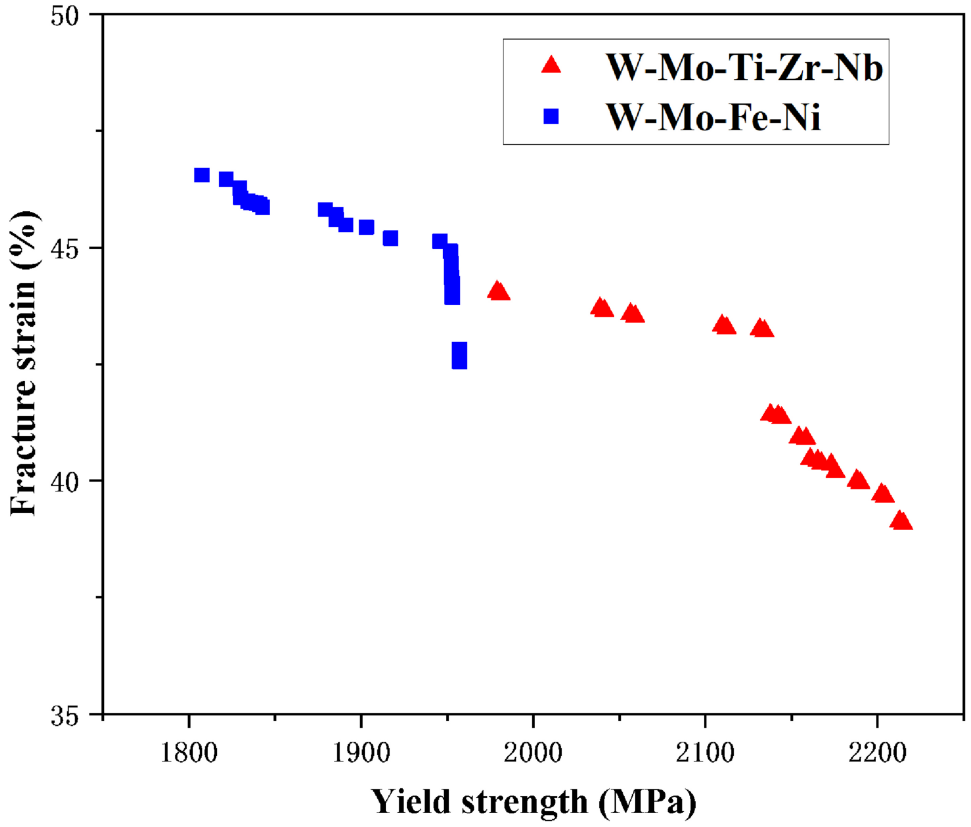


Figure 8. Multi-objective optimization of the Pareto frontier solution set based on the W-Mo-Ti-Zr-Nb system and the W-Mo-Fe-Ni system.

Iterative optimization via master alloy strategy

To address the fabricability challenge while preserving search efficiency, a master alloy strategy was adopted as a hard constraint within the NSGA-II framework. The strategy imposes equiatomic ratios between element pairs with similar melting points: Fe:Ni = 1:1 and W:Mo = 1:1. This facilitates practical fabricability by allowing a two-step process, pre-melting homogeneous Fe-Ni and W-Mo master alloys separately, followed by final co-melting, which reduces the melting-point mismatch between constituent elements without compromising compositional search efficiency. The optimization was then performed in three iterative rounds with progressively refined exploration strategies [Figure 9]. In each iteration, the NSGA-II algorithm systematically screened 250,000 objective evaluations on hypothetical compositions (with a population size of 500 and 500 generations).

First iteration: identifying the fabricability bottleneck. With the equiatomic constraints imposed, the NSGA-II algorithm conducted an initial screening over the W-Mo-Fe-Ni composition space. The resulting Pareto-optimal solutions were overwhelmingly concentrated in the ultra-high W-Mo regime, where the total atomic fraction of W and Mo, defined as the sum of the W and Mo atomic fractions, exceeded 60 at.%.

While these compositions exhibited excellent predicted mechanical properties, experimental realization of such compositions posed significant challenges: the extremely high melting point and limited mutual solubility between W/Mo and Fe/Ni at such concentrations may lead to practical fabrication challenges, such as segregation, incomplete melting, and element loss during arc melting. This outcome highlighted a critical gap between computational prediction and experimental feasibility, motivating a targeted exploration of lower W-Mo regions in subsequent iterations.

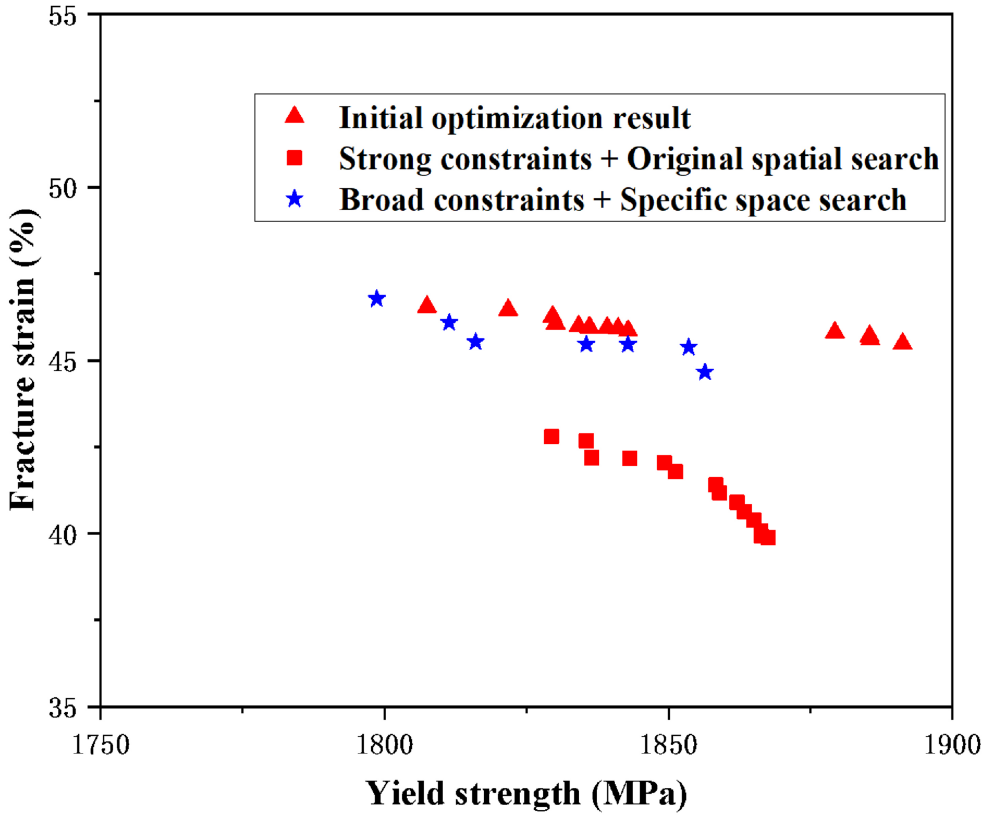


Figure 9. Multi-objective optimization of the Pareto frontier solution set based on the master alloy strategy.

Table 3. Measured densities of selected nominal alloy compositions

Nominal atomic proportion/%				Measured density g/cm³
Fe	Ni	Mo	W	
40.00	40.00	10.00	10.00	9.95
37.00	37.00	13.00	13.00	10.27
33.00	33.00	17.00	17.00	10.64
29.50	29.50	20.50	20.50	11.30

Second iteration: screening in the moderate W-Mo regime. Guided by the first iteration, the optimization search was redirected toward the moderate W-Mo optimization target range (20-50 at.%). The Pareto-optimal solutions from this iteration converged to a well-distributed front covering the entire 20-50 at.% W-Mo range. Five representative compositions with total atomic fractions of W and Mo of 20, 26, 34, 42, and 50 at.% (optimization targets), spanning the full Pareto front, were selected as candidates for experimental validation. During synthesis, the final two compositions were adjusted to nominal values of 41 and 49 at.% [see Section "Validation in the moderate W-Mo regime (nominal total atomic fraction of W and Mo ≤ 49 at.%)"]. Density, calculated using the formula in Table 1, was incorporated as a screening criterion in the NSGA-II optimization (with a threshold of 10 g/cm³); individuals with estimated density below this threshold were excluded from the Pareto front during the non-dominated sorting step (Section "Establishment of multi-objective optimization algorithm"). Subsequently, densities were measured for a subset of the synthesized alloys (Section "Experimental validation", Table 3) to assess consistency with this screening criterion.

Third iteration: exploring the boundary of reliable prediction. To further probe the predictive capability along the same Fe:Ni = W:Mo pathway beyond the trained composition range, a third iteration targeted the $W_{30}Mo_{30}Fe_{20}Ni_{20}$ composition (total atomic fraction of W and Mo = 60 at.%), a representative Pareto-optimal candidate at the boundary with a high total atomic fraction of W and Mo of the explored design space identified in the first iteration.

The experimental validation of both the second-iteration candidates and the third-iteration boundary composition is presented in Section "Experimental validation", where the predictive reliability of model in the well-predicted compositional regime and its limitations at the boundary of reliable prediction are systematically examined.

Experimental validation

To assess the practical effectiveness of the MMOS framework, the candidate compositions identified through the three iterative optimization rounds were synthesized via vacuum arc-melting and tested using an SHPB system. The experimental results serve two purposes: (i) assessing the predictive reliability of the CK-fusion model in the interpolation regime; and (ii) probing the extrapolation limits of the model while revealing an attractive dynamic response at the boundary with a high total atomic fraction of W and Mo of the explored design space.

Although fracture occurred in the specimens during testing, no photographic record of the fracture surfaces was available. The experimental strain values are therefore conservatively reported as the maximum compressive strain attained before unloading (ε_{max}), which represents a lower bound on the true fracture strain.

Validation in the moderate W-Mo regime (nominal total atomic fraction of W and Mo ≤ 49 at.%)

Five representative compositions with total atomic fractions of W and Mo of 20, 26, 34, 41, and 49 at.% (nominal synthesis compositions) were selected as candidates for experimental validation. The NSGA-II optimization initially identified targets of 42 and 50 at.%; the final two compositions were adjusted to nominal values of 41 and 49 at.% during weighing for synthesis. No post-casting compositional analysis [e.g., energy-dispersive X-ray spectroscopy (EDS) or inductively coupled plasma (ICP)] was performed; the reported compositions are therefore nominal values based on the weighing masses. All these compositions follow the same equiatomic ratio pattern (Fe:Ni = 1:1, W:Mo = 1:1) as the training data, providing a controlled compositional pathway for evaluating extrapolation along fixed Fe:Ni and W:Mo ratios, while progressively increasing the total atomic fraction of W and Mo beyond the training range (predominantly distributed between 10-35 at.%). All five as-cast alloys were successfully fabricated via the two-step master-alloy melting route.

Table 3 lists the measured densities of four selected candidate alloys; the 49 at.% alloy was measured but excluded due to excessive uncertainty. The values show a monotonic increase with the total atomic fraction of W and Mo: 9.95 g/cm^3 at 20 at.%, 10.27 g/cm^3 at 26 at.%, 10.64 g/cm^3 at 34 at.%, and 11.30 g/cm^3 at 41 at.%. Within this measured subset, compositions with a total atomic fraction of W and Mo ≥ 26 at.% exceed the 10 g/cm^3 estimated-density screening threshold adopted in this study. This indicates that the density constraint can be satisfied within the moderate W-Mo regime while remaining synthesizable by conventional arc melting.

Figures 10 and 11 compare the experimental dynamic mechanical properties against the CK-fusion model predictions across a range of strain rates. Because systematic fracture evidence was not available for all specimens, all strain measurements are conservatively reported as ε_{max} (maximum compressive strain attained

before unloading) rather than as true fracture strain. Conventional relative errors cannot be computed for strain; instead, a conservative consistency check ($\varepsilon_f \geq \varepsilon_{max}$) is applied.

For yield strength, where measurements are fully observed, the individual relative prediction errors are evaluated. Within the tested regime of the nominal total atomic fraction of W and Mo ≤ 49 at.%, the CK-fusion model provides partial directional guidance: the predicted strength trend is broadly consistent with the experimental trend, but the individual prediction errors are non-negligible and tend to increase with increasing total atomic fraction of W and Mo. For strain, because the experimental values are right-censored lower bounds, a conservative consistency check ($\varepsilon_f \geq \varepsilon_{max}$) is applied. In this regime, a subset of predictions satisfies the consistency criterion, but this reflects the conservative nature of the check rather than quantitative accuracy, because the model tends to predict high fracture strains while the measured ε_{max} values are lower bounds. Because the strain observations are right-censored, a rigorous joint quantitative accuracy rate for both objectives cannot be defined from the present experiments. Overall, within this moderate regime, the model captures the general trade-off trend and successfully guides the identification of high-density candidates that are more compatible with conventional arc melting.

Boundary composition: experimental response and model applicability

To further probe the extrapolation behavior of the current model along the same composition pathway, the third iteration targeted the nominal $W_{30}Mo_{30}Fe_{20}Ni_{20}$ composition (total atomic fraction of W and Mo = 60 at.%), a boundary with a high total atomic fraction of W and Mo composition of the explored design space that lies beyond the better-sampled compositional regime established in the second iteration. This composition follows the same equiatomic ratio pattern (Fe:Ni = 1:1, W:Mo = 1:1) as both the training data and the second-iteration alloys. The prediction failure is therefore consistent with extrapolation beyond the training distribution, though microstructural changes at this extreme composition may also contribute. At this composition with a high total atomic fraction of W and Mo, which lies at the edge of the training-data distribution used to train the model, the underlying microstructure may undergo regime transitions, such as intermetallic precipitation or compositional segregation, that are not captured by the current feature set, which lacks microstructural descriptors.

As shown in Figure 12, the model predictions exhibit significant deviations from experimental values at this composition. For yield strength [Figure 12A], the ML-predicted values are consistently lower than the experimental results, indicating clear under-prediction. For strain [Figure 12B], because the experimental values are right-censored lower bounds (ε_{max}), cases with $\varepsilon_f \geq \varepsilon_{max}$ cannot be interpreted as quantitative over-prediction of the true fracture strain; these cases are only consistent with the observed lower bound. Only cases with $\varepsilon_f < \varepsilon_{max}$ constitute definite under-prediction. At 2,054 s^{-1}, for example, the model predicts 14.5% while the specimen reached 25.0% before unloading, demonstrating a clear boundary failure for the strain target. The different deviation directions for the two properties may suggest that the current feature set does not fully capture the distinct physical mechanisms governing each property at extreme W-Mo concentrations, but this interpretation requires further microstructural investigation. The boundary results presented here were obtained within a single experimental campaign and do not establish batch-to-batch reproducibility. Independent melt-batch validation will be required before generalizing the quantitative response of this composition.

This boundary exploration reveals a fundamental distinction: the MMOS framework successfully converged to a promising composition region ($W_{30}Mo_{30}Fe_{20}Ni_{20}$) where attractive dynamic properties emerge in the as-cast state, even though this specific composition lies outside the reliable prediction domain of the model. The utility of the framework in this regime therefore derives primarily from its exploration efficiency, namely the ability to sample and converge on promising regions, rather than from composition-level prediction

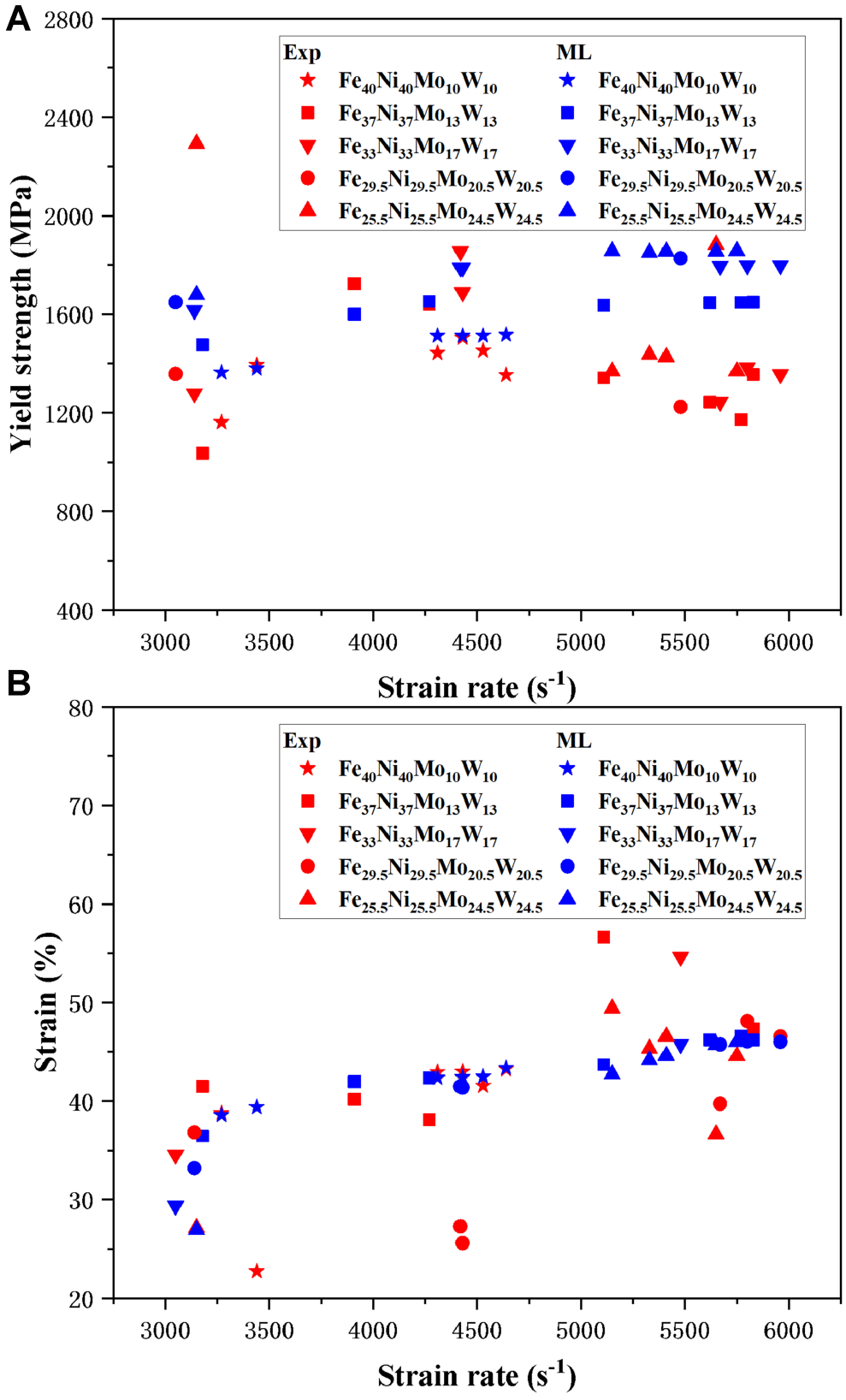


Figure 10. Comparison of experimental values and ML-predicted values for the five synthesized candidate alloys derived from selected second-iteration Pareto targets across the SHPB test matrix: (A) yield strength; (B) strain. Experimental data (Exp) are reported as the maximum compressive strain attained before unloading (ε_{max}; right-censored lower bounds); systematic fracture confirmation was unavailable, and strains are therefore conservatively treated as lower-bound observations. ML predictions (ML) are the model-predicted fracture strains (ε_f). Because the experimental strain values are censored, a conservative consistency check ($\varepsilon_f \geq \varepsilon_{max}$) rather than conventional relative errors is applied. ML: Machine learning; SHPB: split Hopkinson pressure bar.

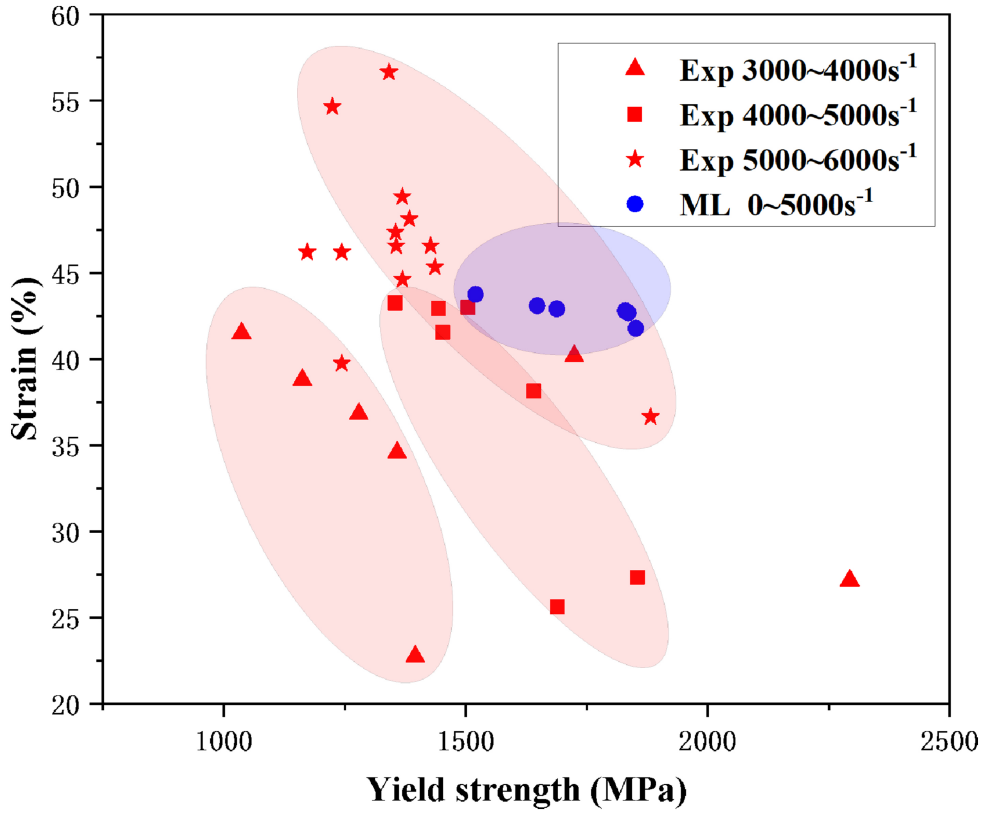


Figure 11. Comparison of the Pareto front solution set obtained from multi-objective optimization with experimental data, classified by strain rate. The Pareto front represents ML-predicted fracture strain (ε_f) *vs.* yield strength. Experimental points (Exp) show the observed maximum compressive strain (ε_{max}; right-censored lower bounds). For strain, the comparison is made only for consistency ($\varepsilon_f \geq \varepsilon_{max}$), not as quantitative validation of fracture-strain predictions, because the experimental values are lower-bound observations. ML: Machine learning.

accuracy for every individual composition.

At a strain rate of 2,054 s^{-1}, the $W_{30}Mo_{30}Fe_{20}Ni_{20}$ as-cast alloy achieved a dynamic compressive yield strength of 2,174 MPa coupled with a maximum compressive strain of 25% [Figure 13A]. Figure 13A provides a qualitative benchmark against selected reported RHEAs from the literature under broadly comparable high-strain-rate conditions. The comparison indicates that the designed alloy falls within the upper-right region, exhibiting a strength-ductility balance that is broadly comparable to many reported RHEAs. It is acknowledged that the strain rates of the literature data are not perfectly identical to the testing conditions, typically ranging from ~10^3 to ~5 × 10^3 s^{-1}. Notably, the alloy achieves 2,174 MPa at a lower strain rate (2,054 s^{-1}) than several literature data points (> 4,000 s^{-1}). This suggests that the alloy compares favorably with the selected literature data, although a direct quantitative comparison is complicated by differences in testing conditions, microstructure, and processing history. The key conclusion remains that the MMOS framework successfully identified a composition with an attractive dynamic-compression response. The engineering stress-strain curves [Figure 13B] further reveal a pronounced work-hardening response prior to unloading, which is qualitatively consistent with the activation of effective deformation mechanisms under dynamic loading; however, the specific mechanisms require systematic microstructural characterization in future work.

First, despite the prediction failure at the 60 at.% W-Mo boundary, the multi-objective optimization framework successfully navigated the vast compositional space to identify an as-cast composition with a high total atomic fraction of W and Mo where attractive dynamic properties emerge directly after solidification.

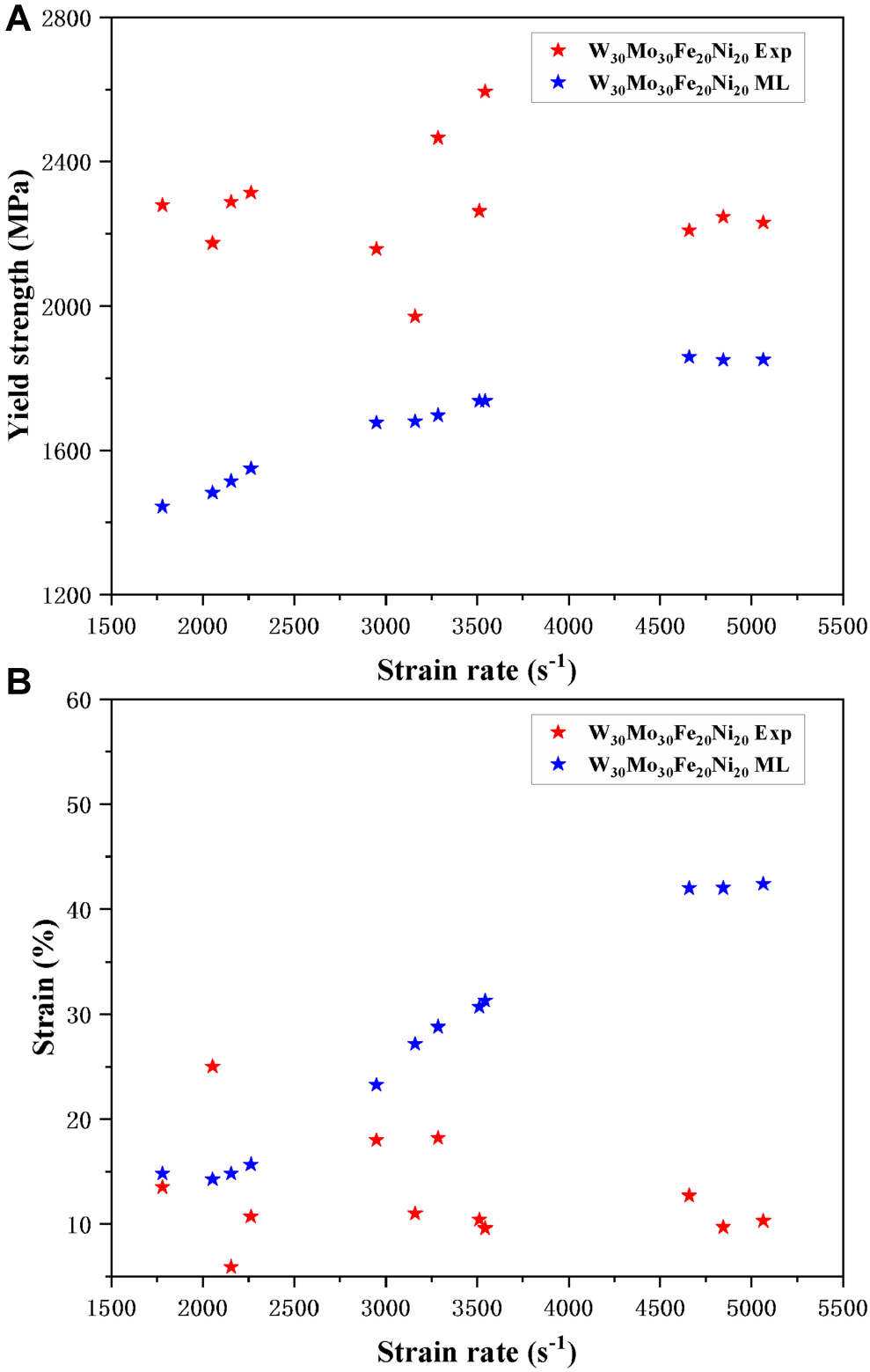


Figure 12. Comparison of experimental and ML-predicted mechanical properties for the boundary composition $W_{30}Mo_{30}Fe_{20}Ni_{20}$ (total atomic fraction of W and Mo = 60 at.%): (A) yield strength; (B) strain. Experimental strain values (Exp) are the maximum compressive strain attained before unloading (ε_{max}; right-censored lower bounds). ML predictions (ML) are the model-predicted fracture strains (ε_f). This composition lies outside the reliable interpolation domain of the model; the deviations delineate the applicability boundary of the current model. ML: Machine learning.

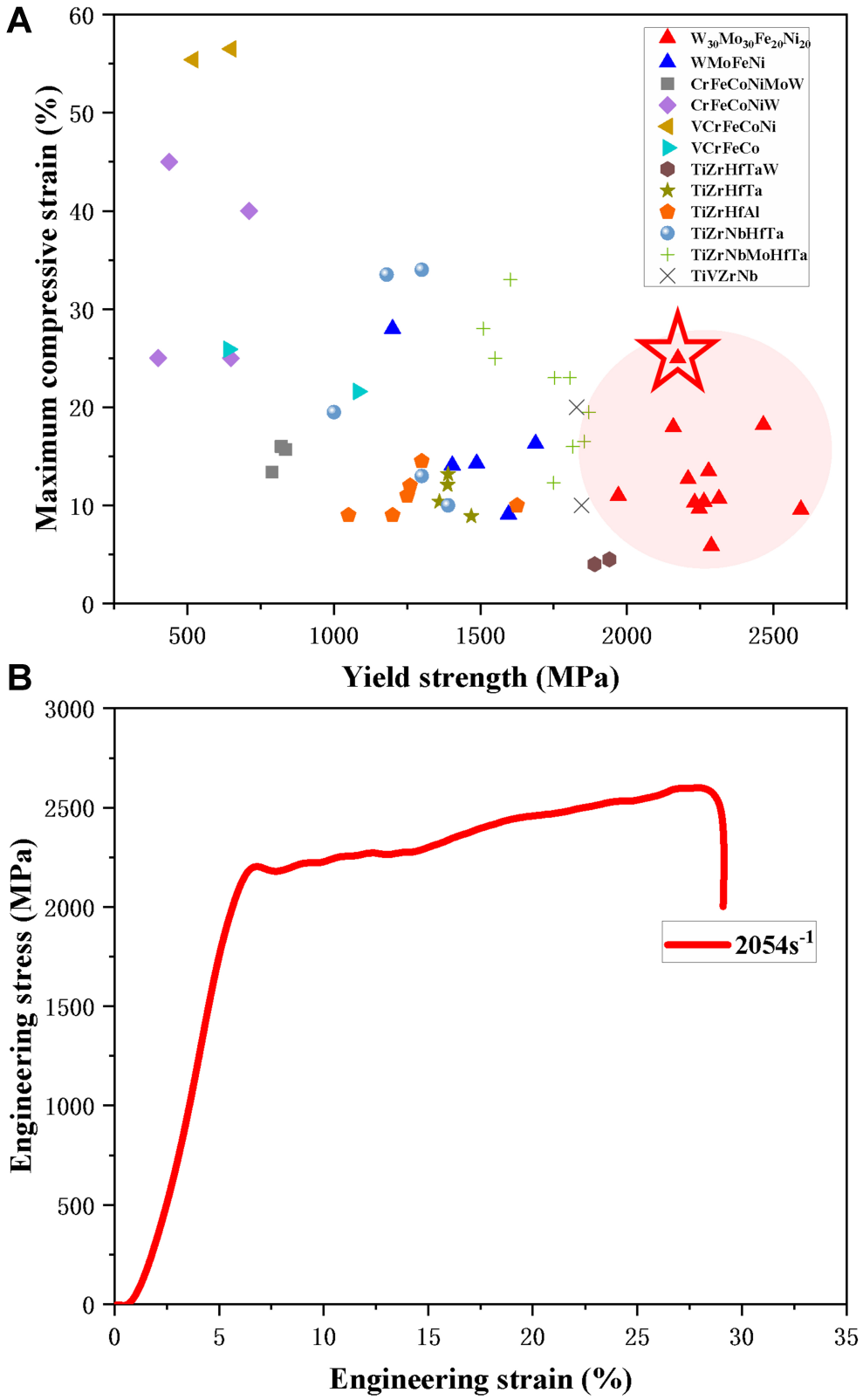


Figure 13. The $W_{30}Mo_{30}Fe_{20}Ni_{20}$ alloy: (A) comparison of dynamic mechanical properties (yield strength *vs.* maximum compressive strain) between the Pareto-optimal $W_{30}Mo_{30}Fe_{20}Ni_{20}$ alloy and selected reported RHEAs from the literature[63-75] under high-strain-rate conditions, where the large red five-pointed star marks the experimental data point of the $W_{30}Mo_{30}Fe_{20}Ni_{20}$ alloy at 2,054 s^{-1}; (B) engineering stress-strain curve of the $W_{30}Mo_{30}Fe_{20}Ni_{20}$ alloy at the strain rate of 2,054 s^{-1}; the star in (A) denotes the triplicate mean at 2,054 s^{-1}; (B) shows a representative stress-strain curve. RHEAs: Refractory high-entropy alloys.

The value of the framework therefore lies not solely in prediction accuracy, but more fundamentally in its exploration efficiency, the ability to efficiently sample and converge on promising regions of the performance landscape, even at the limits of model reliability. Second, the observed prediction failure clearly delineates the applicability domain of the current model, providing a concrete direction for future improvement: incorporating quantitative microstructural descriptors (e.g., phase fraction, grain size, precipitate morphology) and expanding the training database into the under-sampled region beyond a total atomic fraction of W and Mo of 50 at.% are essential for extending the applicability of the framework. Third, this work establishes a foundation for future closed-loop development by completing the first complete design-and-validation cycle. The experimental data generated at the boundary of the model, including both the experimentally characterized cases in the nominal total atomic fraction of W and Mo ≤ 49 at.% tested regime and the systematic deviations observed at total atomic fraction of W and Mo = 60 at.%, have not yet been used to retrain and prospectively retest the model, as such an iterative cycle lies beyond the scope of the present study. However, these data have been archived as an experimental feedback dataset for future incorporation into an expanded training database and provide the basis for the subsequent iteration of model refinement. This progressive accumulation of empirical feedback, building toward a fully closed-loop paradigm, provides the basis for future refinement of the framework. The present work reports a complete design-and-validation cycle, from computational screening to SHPB validation, establishing a foundation for future closed-loop development, while delineating the current limitations of the framework.

CONCLUSIONS

In this work, a knowledge-enabled, data-driven multi-objective optimization framework (MMOS) was developed to accelerate the discovery of WW-RHEAs with attractive dynamic mechanical properties. The following conclusions can be drawn:

(1) A systematic comparison of three feature strategies, composition-only (C), knowledge-only (K), and composition + knowledge (CK), revealed that CK is most effective when paired with the ExtraTrees algorithm, achieving the highest predictive accuracy among all evaluated models. While CK is not universally dominant across all algorithms, the ExtraTrees + CK combination yielded the best overall performance and was therefore selected as the optimal model for subsequent optimization. SHAP provides model-based associations that offer plausible mechanistic interpretations of this superiority: compositional features (e.g., Cr, Ni, Al) show substantial associations with strength prediction, which is qualitatively consistent with the expected role of solid-solution strengthening in RHEAs; whereas knowledge features, particularly strain rate, Young's modulus, and B/G, show strong associations with ductility prediction, suggesting that these physically meaningful descriptors capture aspects of the complex mechanisms governing plastic deformation and fracture. This mechanism-dependent importance underscores that feature selection must be tailored to both the target property and the alloy system.

(2) The ExtraTrees algorithm with the CK fusion feature set achieved a test R^2 of 0.96 for dynamic yield strength and 0.87 for fracture strain. By embedding these predictive models into the NSGA-II framework and incorporating equiatomic composition constraints (Fe:Ni = 1:1, W:Mo = 1:1) based on a master alloy strategy, the optimization efficiently performed 250,000 objective evaluations on hypothetical compositions in each of three iterative rounds with progressively refined exploration strategies, enhancing search efficiency while incorporating practical fabricability considerations for conventional arc melting.

(3) Experimental validation via SHPB testing demonstrated the practical utility of the framework. The optimization converged to the $W_{30}Mo_{30}Fe_{20}Ni_{20}$ alloy as a promising candidate, which achieved 2,174 MPa dynamic compressive yield strength and 25% maximum compressive strain (ε_{max}) at 2,054 s^{-1}, an attractive dynamic-compression response. In the interpolation regime, the CK-fusion model provided partial

directional screening guidance; at the boundary with a high total atomic fraction of W and Mo, its quantitative predictive capability degraded markedly. These deviations delineate the applicability domain of the model and point to future improvement through the incorporation of microstructural descriptors and expansion of the training database into the under-sampled high W-Mo regime. The primary strength of the MMOS framework therefore lies in exploration efficiency rather than composition-level prediction accuracy.

(4) This work establishes a foundation for closed-loop design-to-validation development, completing a full design-and-validation cycle that integrates data-driven exploration, model-based interpretability, and experimental characterization. While the new experimental data have not yet been used for model retraining and prospective retesting, which is reserved for future iterations, the present study demonstrates the practical utility of the MMOS framework and provides a clear pathway toward progressively expanding the reliable design space through successive computational-experimental cycles.

DECLARATIONS

Authors' contributions

Contributed to conceptualization, methodology, software, investigation, formal analysis, and writing - original draft: Gao, Y.
Helped with methodology and writing - review and editing: Jia, D.
Involved in data curation and methodology: Zhang, R.
Contributed to investigation and validation: Fan, Y.
Supervised the work and provided resources: Tang, Y.
Supervised the work, provided resources, and assisted in writing - review and editing: Wang, W. Y.
Provided resources and supervision: Bai, S.
Supervised the work, administered the project, and provided resources: Li, J.

Availability of data and materials

The original contributions presented in this study are included in the article/Supplementary Materials. Further inquiries can be directed to the corresponding author(s).

AI and AI-assisted tools statement

During the preparation of this manuscript, the AI tool DeepSeek (version R1, released 2025-01-20) was used for language editing. The AI tool Dola (version 2.0, released 2024-05-15) from TikTok was used to generate or assist with certain icons. In Figure 1, the AI-assisted icon is the model symbol (the "Model" icon). In the Graphical Abstract, the AI-assisted icons are the yield strength, density, and fracture strain icons in the first part. No AI tools were used for the data plots or scientific content in Figures 2-13. The tools did not influence the study design, data collection, data analysis, interpretation, or the scientific content of the work. All authors take full responsibility for the accuracy, integrity, and final content of the manuscript.

Financial support and sponsorship

This work was financially supported by the National Defense Basic Scientific Research Program (Grant No. 2022-JCJQ-JJ-0002-02).

Conflicts of interest

Wang, W. Y. is an Editorial Board Member of the journal *Journal of Materials Informatics*. Wang, W. Y. was not involved in any steps of editorial processing, notably including reviewers' selection, manuscript handling and decision-making. The other authors declare that there are no conflicts of interest.

Ethical approval and consent to participate

Not applicable.

Consent for publication

Not applicable.

Copyright
© The Author(s) 2026.

Supplementary Materials
Supplementary Materials

REFERENCES

1. Behner, T.; Heine, A.; Wickert, M. Dwell and penetration of tungsten heavy alloy long-rod penetrators impacting unconfined finite-thickness silicon carbide ceramic targets. *Int. J. Impact. Eng.* **2016**, *95*, 54-60. DOI
2. Cury, R.; Issartel, F.; Joubert, J.; Couque, H. Evolution of cobalt-free tungsten heavy alloys for kinetic energy penetrators. *Powder. Metall.* **2013**, *56*, 347-50. DOI
3. Luo, R.; Huang, D.; Yang, M.; Tang, E.; Wang, M.; He, L. Penetrating performance and "self-sharpening" behavior of fine-grained tungsten heavy alloy rod penetrators. *Mater. Sci. Eng. A.* **2016**, *675*, 262-70. DOI
4. Fang, X.; Liu, J.; Wang, X.; Li, S.; Guo, W. Investigation on the penetration performance and "self-sharpening" behavior of the 80W–14Cu–6Zn penetrators. *Int. J. Refract. Met. Hard. Mater.* **2016**, *54*, 237-43. DOI
5. Zhu, F.; Chen, Y.; Zhu, G. Numerical simulation study on penetration performance of depleted Uranium (DU) alloy fragments. *Def. Technol.* **2021**, *17*, 50-5. DOI
6. Bleise, A.; Danesi, P. R.; Burkart, W. Properties, use and health effects of depleted uranium (DU): a general overview. *J. Environ. Radioact.* **2003**, *64*, 93-112. DOI
7. Wang, B.; Dong, Y.; Huang, G. An investigation on the adiabatic shear bands in depleted U-0.75 wt % Ti alloy under dynamic loading. *Metals* **2018**, *8*, 145. DOI
8. Meyers, M. A. *Dynamic behavior of materials*. Wiley & Sons, Inc., 1994. https://books.google.com/books/about/Dynamic_Behavior_of_Materials.html?id=WoEDHtRTOhoC. (accessed 2026-10-10).
9. Kim, D.; Lee, S.; Hyung Baek, W. Microstructural study of adiabatic shear bands formed by high-speed impact in a tungsten heavy alloy penetrator. *Mater. Sci. Eng. A.* **1998**, *249*, 197-205. DOI
10. Arfsten, D. P.; Still, K. R.; Ritchie, G. D. A review of the effects of uranium and depleted uranium exposure on reproduction and fetal development. *Toxicol. Ind. Health.* **2001**, *17*, 180-91. DOI PubMed
11. Yeh, J.; Chen, S.; Lin, S.; et al. Nanostructured high-entropy alloys with multiple principal elements: novel alloy design concepts and outcomes. *Adv. Eng. Mater.* **2004**, *6*, 299-303. DOI
12. Wang, F.; Song, M.; Wang, Z. Advanced lightweight Fe-Mn-Al-Ni-C compositionally complex steels: alloy design, microstructural evolution, and deformation mechanisms. *Mets. Adv.* **2026**, *47*, 1-9. DOI
13. Senkov, O.; Wilks, G.; Miracle, D.; Chuang, C.; Liaw, P. Refractory high-entropy alloys. *Intermetallics* **2010**, *18*, 1758-65. DOI
14. Wang, J.; Zhou, M.; Zhu, L.; Kong, L.; Tan, X.; Li, J. Synergistic effects of Hf and Ta on strength-ductility in refractory high-entropy alloys: kink band formation and dislocation evolution. *Acta. Mater.* **2025**, *300*, 121492. DOI
15. Wang, R.; Fan, Y.; Chen, R.; et al. Enhancing strain hardening and strength-plasticity synergy upon dynamic loads in refractory high-entropy alloys via B2 ordering and spinodal decomposition. *Int. J. Plast.* **2025**, *194*, 104482. DOI
16. Li, Z.; Su, B.; Liu, C.; et al. Dislocation behavior and slip plane preferences in refractory multi-principal element alloys: insights into strength-ductility trade-offs. *J. Mater. Sci. Technol.* **2026**, *248*, 199-211. DOI
17. Zhang, W.; Lai, S.; Jiao, B.; et al. Hf-induced transition in deformation mechanism enhances dynamic performance of NbTaTiZr refractory high-entropy alloy. *Mater. Design.* **2026**, *262*, 115498. DOI
18. Wang, Y.; He, Q.; Ye, Z.; et al. Ductilization of single-phase refractory high-entropy alloys via activation of edge dislocation. *Acta. Mater.* **2025**, *284*, 120614. DOI
19. He, J.; Li, Z.; Li, L.; et al. An *in-situ* study on the formation mechanism of adiabatic shear band in refractory high-entropy alloys. *Acta. Mater.* **2026**, *306*, 121843. DOI
20. Wu, S.; Liu, Y.; Ying, H.; et al. Exceptional impact resistance of a high-entropy alloy governed by abnormally active dislocation behavior. *Acta. Mater.* **2026**, *309*, 122079. DOI
21. Lee, C.; Neelakandan, D. P.; Xie, D.; et al. Deformation behaviors in single BCC-phase refractory multi-principal element alloys under dynamic conditions. *Adv. Sci.* **2025**, *12*, e08180. DOI PubMed PMC
22. Fu, A.; Liu, B.; Li, Z.; et al. Superb impact resistance of nano-precipitation-strengthened high-entropy alloys. *Adv. Powder. Mater.* **2025**, *4*, 100277. DOI
23. Khan, M. A.; Wang, J.; Brechtl, J.; et al. Unveiling the dynamic mechanical behavior with phase-transformation and microstructural evolution in a novel dual-phase high-entropy alloy. *Mater. Design.* **2025**, *257*, 114485. DOI

24. Chen, B.; Zheng, F.; Li, J.; et al. Development of ductile refractory alloys with excellent high-temperature strength for extreme environments. *Adv. Mater.* **2026**, *38*, e15947. DOI PubMed
25. An, Z.; Li, A.; Mao, S.; et al. Negative mixing enthalpy solid solutions deliver high strength and ductility. *Nature* **2024**, *625*, 697-702. DOI PubMed
26. Wang, H.; Yang, P. Y.; Zhao, W. J.; et al. Lattice distortion enabling enhanced strength and plasticity in high entropy intermetallic alloy. *Nat. Commun.* **2024**, *15*, 6782. DOI PubMed PMC
27. Fan, L.; Wei, Z.; Tian, Y.; et al. Taming intermediate-temperature brittleness in additively manufactured multi-component alloys via dual-effect alloying. *Acta. Mater.* **2026**, *308*, 121992. DOI
28. Zhang, J.; Xu, X.; Körmann, F.; et al. Lattice distortions and non-sluggish diffusion in BCC refractory high entropy alloys. *Acta. Mater.* **2025**, *297*, 121283. DOI
29. Natarajan, A. R.; Van der Ven, A. Linking electronic structure calculations to generalized stacking fault energies in multicomponent alloys. *npj. Comput. Mater.* **2020**, *6*, 348. DOI
30. Wei, S.; Kim, S. J.; Kang, J.; et al. Natural-mixing guided design of refractory high-entropy alloys with as-cast tensile ductility. *Nat. Mater.* **2020**, *19*, 1175-81. DOI
31. Verma, V.; Belcher, C. H.; Apelian, D.; Lavernia, E. J. Diffusion in high entropy alloy systems - a review. *Prog. Mater. Sci.* **2024**, *142*, 101245. DOI
32. Tang, Y.; Wang, H.; Ouyang, X.; et al. Overcoming strength-ductility tradeoff with high pressure thermal treatment. *Nat. Commun.* **2024**, *15*, 3932. DOI PubMed PMC
33. Kim, I. H.; Oh, H. S.; Lee, K. S.; Park, E. S. Optimization of conflicting properties via engineering compositional complexity in refractory high entropy alloys. *Scr. Mater.* **2021**, *199*, 113839. DOI
34. Zhichao, L.; Dong, M.; Xiongjun, L.; Lu, Z. High-throughput and data-driven machine learning techniques for discovering high-entropy alloys. *Commun. Mater.* **2024**, *5*, 487. DOI
35. Zhang, Y.; Wen, C.; Dang, P.; Lookman, T.; Xue, D.; Su, Y. Toward ultra-high strength high entropy alloys via feature engineering. *J. Mater. Sci. Technol.* **2024**, *200*, 243-52. DOI
36. Liu, X.; Zhang, J.; Pei, Z. Machine learning for high-entropy alloys: progress, challenges and opportunities. *Prog. Mater. Sci.* **2023**, *131*, 101018. DOI
37. Conway, P. L.; Klaver, T.; Steggo, J.; Ghassemali, E. High entropy alloys towards industrial applications: high-throughput screening and experimental investigation. *Mater. Sci. Eng. A.* **2022**, *830*, 142297. DOI
38. Cheng, M.; Fu, C. L.; Okabe, R.; et al. Artificial intelligence-driven approaches for materials design and discovery. *Nat. Mater.* **2026**, *25*, 174-90. DOI
39. Wu, L.; Li, T. A machine learning interatomic potential for high entropy alloys. *J. Mech. Phys. Solids.* **2024**, *187*, 105639. DOI
40. Guduru, S. P. R.; Kekung, M. O.; Ott, R. T.; Roy, S.; Singh, P. DuctGPT: a generative transformer for forward screening of ductile refractory multi-principal element alloys. *Acta. Mater.* **2026**, *304*, 121763. DOI
41. Wang, W.; Abu-Odeh, A. A.; Cook, D. H.; Ritchie, R. O.; Asta, M.; Rao, S. A theoretical study of solid solution strengthening in the refractory medium entropy alloy $Nb_{45}Ta_{25}Ti_{15}Hf_{15}$. *Mater. Design.* **2026**, *261*, 115368. DOI
42. Sohail, Y.; Zhang, C.; Xue, D.; et al. Machine-learning design of ductile FeNiCoAlTa alloys with high strength. *Nature* **2025**, *643*, 119-24. DOI PubMed PMC
43. Wen, C.; Shen, H.; Tian, Y.; Lou, G.; Wang, N.; Su, Y. Accelerated discovery of refractory high-entropy alloys for strength-ductility co-optimization: an exploration in NbTaZrHfMo system by machine learning. *Scr. Mater.* **2024**, *252*, 116240. DOI
44. Li, Z.; Li, S.; Birbilis, N. A machine learning-driven framework for the property prediction and generative design of multiple principal element alloys. *Mater. Today. Commun.* **2024**, *38*, 107940. DOI
45. Luo, M.; Xie, Z.; Li, H.; et al. Physics-informed, dual-objective optimization of high-entropy-alloy nanozymes by a robotic AI chemist. *Matter* **2025**, *8*, 102009. DOI
46. Li, X.; Shan, G.; Zhang, J.; Shek, C. Accelerated design for magnetic high entropy alloys using data-driven multi-objective optimization. *J. Mater. Chem. C.* **2022**, *10*, 17291-302. DOI
47. Gao, T.; Gao, J.; Yang, S.; Zhang, L. Data-driven design of novel lightweight refractory high-entropy alloys with superb hardness and corrosion resistance. *npj. Comput. Mater.* **2024**, *10*, 1457. DOI
48. Zhong, K.; Wu, S.; Liu, S.; Qi, J.; Cheng, L.; Ai, D. Machine learning-driven optimization of hardness and toughness in high-entropy alloy coatings based on composition and descriptor. *J. Appl. Phys.* **2025**, *137*, 195305. DOI
49. Xiao, X.; Wang, Z.; Yun, P.; et al. An interatomic-energy-based new materials design strategy combining DFT calculations and active machine learning. *J. Mater. Sci. Technol.* **2026**, *267*, 13-22. DOI
50. Xu, P.; Ma, Y.; Lu, W.; Li, M.; Zhao, W.; Dai, Z. Multi-objective optimization in machine learning assisted materials design and discovery. *J. Mater. Inf.* **2025**, *5*, 26. DOI

51. Toor, Z. S.; Wu, R.; Hashmi, M. R.; et al. Computation- and process-based design for advanced structural high-entropy alloy development and analyses: a critical review. *Prog. Mater. Sci.* **2026**, *155*, 101534. DOI
52. Wang, T.; Li, J.; Wang, M.; et al. Unraveling dislocation-based strengthening in refractory multi-principal element alloys. *npj. Comput. Mater.* **2024**, *10*, 1330. DOI
53. Feng, L.; Jin, G.; Cui, X.; et al. Optimizing laser cladding process parameters for transformation-induced plasticity FeMnCoCr high entropy alloy: a multi-objective approach. *Surf. Coat. Technol.* **2025**, *495*, 131536. DOI
54. Liao, R.; Li, Y.; Ye, Z.; et al. Achieving exceptional strength-ductility synergy in transition metal high-entropy alloys via machine learning-assisted multi-objective optimization. *J. Alloys. Compd.* **2026**, *1059*, 187111. DOI
55. Poluru, S.; Jaimin, A.; Kotkunde, N. R.; et al. Constitutive modelling and microstructural analysis of 92W-5Co-3Ni alloy subjected to high strain rate testing at elevated temperatures. *Mater. Design.* **2025**, *254*, 114035. DOI
56. Huang, H.; Singh, P.; Johnson, D. D.; et al. Achieving high tensile strength and ductility in refractory alloys by tuning electronic structure. *Nat. Mater.* **2026**, *25*, 386-94. DOI
57. Zhang, R.; Wang, W. Y.; Fan, Y.; et al. Knowledge-enabled data-driven smart design advanced high-entropy alloys with attractive dynamic mechanical properties. *J. Mater. Sci.* **2025**, *60*, 567-87. DOI
58. Deb, K.; Pratap, A.; Agarwal, S.; Meyarivan, T. A fast and elitist multiobjective genetic algorithm: NSGA-II. *IEEE. Trans. Evol. Computat.* **2002**, *6*, 182-97. DOI
59. Liu, S.; Fan, X.; Ye, H.; et al. Knowledge-enabled data-driven smart design of ultra-strong ductile near-α titanium alloys under extreme conditions. *J. Mater. Inf.* **2026**, *6*, 18. DOI
60. Kerner, J.; Dogan, A.; von Recum, H. Machine learning and big data provide crucial insight for future biomaterials discovery and research. *Acta. Biomater.* **2021**, *130*, 54-65. DOI PubMed
61. Meyers, M. A.; Chawla, K. K. *Mechanical behavior of materials*, 2nd ed.; Cambridge University Press, 2009. https://ceimusb.wordpress.com/wp-content/uploads/2015/04/mechanicalbehaviormeyers.pdf. (accessed 2026-10-10).
62. McEwen, L. R. *CRC Handbook of chemistry and physics*, 107th ed.; CRC Press, 2026. https://www.routledge.com/CRC-Handbook-of-Chemistry-and-Physics/McEwen/p/book/9781041194620. (accessed 2026-10-10).
63. Chen, H.; Zhang, X.; Dai, L.; Liu, C.; Xiong, W.; Tan, M. Experimental study on WFeNiMo high-entropy alloy projectile penetrating semi-infinite steel target. *Def. Technol.* **2022**, *18*, 1470-82. DOI
64. Zhang, S.; Wang, Z.; Yang, H.; Qiao, J.; Wang, Z.; Wu, Y. Ultra-high strain-rate strengthening in ductile refractory high entropy alloys upon dynamic loading. *Intermetallics* **2020**, *121*, 106699. DOI
65. Hu, M.; Song, W.; Duan, D.; Wu, Y. Dynamic behavior and microstructure characterization of TaNbHfZrTi high-entropy alloy at a wide range of strain rates and temperatures. *Int. J. Mech. Sci.* **2020**, *182*, 105738. DOI
66. Chen, J.; Chen, C.; Guo, K.; et al. Dynamic mechanical properties and ignition behavior of $TiZrHfX_{0.5}$ high-entropy alloys associated with temperature, trace element and strain rate. *J. Alloys. Compd.* **2023**, *933*, 167798. DOI
67. Huang, Y.; Xie, Z.; Li, W.; Chen, H.; Liu, B.; Wang, B. Dynamic mechanical properties of the selective laser melting $NiCrFeCoMo_{0.2}$ high entropy alloy and the microstructure of molten pool. *J. Alloys. Compd.* **2022**, *927*, 167011. DOI
68. Jo, Y.; Kim, D.; Jo, M.; et al. Effects of deformation–induced BCC martensitic transformation and twinning on impact toughness and dynamic tensile response in metastable VCrFeCoNi high–entropy alloy. *J. Alloys. Compd.* **2019**, *785*, 1056-67. DOI
69. Zhou, S.; Jian, R.; Liang, Y.; et al. High susceptibility to adiabatic shear banding and high dynamic strength in tungsten heavy alloys with a high-entropy alloy matrix. *J. Alloys. Compd.* **2021**, *859*, 157796. DOI
70. Liu, X.; Wu, Y.; Wang, Y.; et al. Enhanced dynamic deformability and strengthening effect via twinning and microbanding in high density NiCoFeCrMoW high-entropy alloys. *J. Mater. Sci. Technol.* **2022**, *127*, 164-76. DOI
71. Tang, W.; Zhang, K.; Chen, T.; Wang, Q.; Wei, B. Microstructural evolution and energetic characteristics of $TiZrHfTa_{0.7}W_{0.3}$ high-entropy alloy under high strain rates and its application in high-velocity penetration. *J. Mater. Sci. Technol.* **2023**, *132*, 144-53. DOI
72. Zhang, Z.; Zhang, H.; Tang, Y.; et al. Microstructure, mechanical properties and energetic characteristics of a novel high-entropy alloy $HfZrTiTa_{0.53}$. *Mater. Design.* **2017**, *133*, 435-43. DOI
73. Dirras, G.; Couque, H.; Lilensten, L.; et al. Mechanical behavior and microstructure of $Ti_{20}Hf_{20}Zr_{20}Ta_{20}Nb_{20}$ high-entropy alloy loaded under quasi-static and dynamic compression conditions. *Mater. Charact.* **2016**, *111*, 106-13. DOI
74. Ren, K.; Liu, H.; Chen, R.; et al. Compression properties and impact energy release characteristics of TiZrNbV high-entropy alloy. *Mater. Sci. Eng. A.* **2021**, *827*, 142074. DOI
75. Song, H.; Kim, D. G.; Kim, D. W.; et al. Effects of strain rate on room- and cryogenic-temperature compressive properties in metastable $V_{10}Cr_{10}Fe_{45}Co_{35}$ high-entropy alloy. *Sci. Rep.* **2019**, *9*, 6163. DOI PubMed PMC

Disclaimer/Publisher's Note: All statements, opinions, and data contained in this publication are solely those of the individual author(s) and contributor(s) and do not necessarily reflect those of OAE and/or the editor(s). OAE and/or the editor(s) disclaim any responsibility for harm to persons or property resulting from the use of any ideas, methods, instructions, or products mentioned in the content.



© The Author(s) 2026. Open Access This article is licensed under a Creative Commons Attribution 4.0 International License (https://creativecommons.org/licenses/by/4.0/), which permits unrestricted use, sharing, adaptation, distribution and reproduction in any medium or format, for any purpose, even commercially, as long as you give appropriate credit to the original author(s) and the source, provide a link to the Creative Commons license, and indicate if changes were made.